

# A Method for Estimating the Physical and Acoustic Properties of the Sea Bed Using Chirp Sonar Data

Steven G. Schock, *Member, IEEE*

**Abstract**—This paper proposes a method, based on the Biot model, for estimating the physical and acoustic properties of surficial ocean sediments from normal incidence reflection data acquired by a chirp sonar. The inversion method estimates sediment porosity from reflection coefficient measurements and, using the estimated porosity and the measured change in fast wave attenuation with frequency, estimates the permeability of the top sediment layer. The spectral ratio of echoes from the interface at the base of the upper sediment layer and from the sediment–water interface provides a measure of the change in attenuation with frequency. Given the porosity and permeability estimates, the Kozeny-Carman equation provides the mean grain size and the inversion method yields the acoustic properties of top sediment layer. The inversion technique is tested using chirp sonar data collected at the 1999 Sediment Acoustics Experiment (SAX-99) site. Remote estimates of porosity, grain size, and permeability agree with direct measurements of those properties.

**Index Terms**—Attenuation, Biot model, chirp sonar, sediment classification.

## I. INTRODUCTION

A METHOD for estimating the acoustic and physical properties of the uppermost layer in the sea bed from reflection profiler data is developed using Biot theory and is tested using chirp sonar data and physical property measurements of sands collected during the 1999 Sediment Acoustic Experiment (SAX-99) conducted off Fort Walton Beach, FL. A chirp sonar transmits frequency-modulation (FM) pulses over the band of 1–15 kHz and acquires reflection data at normal incidence to the sea bed using one transmitter and one receiver collocated in a towed sonar vehicle. The reflection coefficient is measured using the average intensity of the sediment–water interface echo. The reflection coefficient is strongly correlated with sediment porosity and bulk density, so it can be used to estimate those bulk properties. However, the porosity and reflection coefficient are weakly related to grain size and permeability, so a second remote acoustic measurement, the attenuation rolloff measurement, is used to estimate mean grain size and permeability.

Attenuation rolloff (in decibels per meter per kilohertz) is the slope of the amplitude spectrum of an echo from the lower boundary of the uppermost sediment layer divided by the amplitude spectrum of the sediment–water interface echo.

Manuscript received July 10, 2003; revised November 24, 2004. This work was supported by the U.S. Office of Naval Research under Grant N00014-00-1-0847.

The author is with the Department of Ocean Engineering, Florida Atlantic University, Boca Raton, FL 33431 USA (e-mail: schock@oe.fau.edu).

Digital Object Identifier 10.1109/JOE.2004.841421

Consequently, the attenuation rolloff is approximately equal to the slope of the attenuation (in decibels per meter) versus frequency function for the acoustic wave traveling in that layer. This paper describes the procedure for using reflection coefficient and attenuation rolloff measurements and the Biot model to calculate the physical and acoustic properties of the top layer of sediments.

The complex reflection coefficient is defined by

$$R = \frac{P_r}{P_i} \quad (1)$$

where  $P_i$  and  $P_r$  are the complex amplitudes of the incident and reflected waves measured just above the sediment–water interface. The reflection level, which is the negative of the bottom loss, is measured using

$$RL = -BL = 20 \log R = 10 \log \frac{\langle |P_r|^2 \rangle}{|P_i|^2} \quad (2)$$

where  $\langle |P_r|^2 \rangle$  is the squared pressure amplitude of the reflected wave averaged over many acoustic transmissions.

Hamilton [1] and Chotiros [2] summarize investigations that compare bottom-loss measurements and sediment properties. Hamilton describes a viscous-elastic model that provides interrelationships between reflection coefficient measurements and sediment properties. In the viscous-elastic model, the reflection coefficient is related to bottom properties by

$$R = \frac{z_2 - z_1}{z_2 + z_1} \quad (3)$$

where  $z_1$  is the acoustic impedance of seawater and  $z_2$  is the acoustic impedance of sediments. Hamilton uses (3) to generate interrelationships between bottom loss and sediment porosity and bulk density. Chotiros [2] compares bottom-loss measurements and reflection losses calculated from sediment properties using both the Biot and viscous-elastic models for sound propagation in sediments. The study shows that the Biot model correctly predicts the bottom losses for sandy sea beds, while the viscous-elastic model (3) predicts bottom losses that are 1–2 dB lower than measured bottom losses. The viscous-elastic model does not account for the energy loss associated with the creation of a Biot slow wave at the sediment–water interface.

Several field studies support the application of the Biot model to ocean sediments. The Biot model requires 13 input parameters to calculate fast and shear wave velocities and attenuations. Holland [3] uses only two measured parameters, porosity and grain size, to calculate the other 11 input parameters and the

model outputs of wave speed and attenuation at three shallow-water sites in the Mediterranean. The computed velocities and attenuations agree with fast wave velocity and attenuation measurements at 400 Hz and shear wave velocity measurements in the band of 5–15 Hz.

Williams [4] tests the Biot model using fast wave attenuation and velocity measurements of the sandy sea bed at the SAX-99 site off Fort Walton Beach, FL. A variety of *in situ* and remote acoustic techniques provide fast wave attenuation and velocity measurements covering the band of 125 Hz–400 kHz. The model predictions agree with the measurements except for attenuation measurements using frequencies above 100 kHz. Volume scattering, which increases the transmission loss above that caused by intrinsic attenuation, is a potential cause for the measured attenuation being significantly higher than the attenuation predicted by the Biot model.

Chotiros [5] reports the presence of slow and fast Biot waves traveling in the sandy sediments. During experiments offshore of Panama City, FL, and Jacksonville, FL, an acoustic source transmitted continuous-wave (CW) and FM pulses covering the band from 5 to 80 kHz. Arrays of buried hydrophones measured the speed and attenuation of slow and fast waves. The measured fast wave speeds are about 1700 m/s, while the slow wave speeds are about 1200 m/s. Chotiros reports that increasing the frame bulk modulus by a factor of 50 and decreasing the grain bulk modulus by a factor of 5 from values used by other investigators provides a better fit between the measured attenuation of slow and fast waves and the attenuation predicted by the Biot model. This discrepancy suggests that the Biot model needs modification.

Chotiros [6] presents a method for calculating the frame shear modulus and log decrement, the frame bulk modulus and log decrement, and the grain bulk modulus from measurements of acoustic and physical sediment properties. The inputs for the inversion model are measurements of shear and fast wave speeds, shear and fast wave attenuation, reflection loss, porosity, grain density, and pore fluid density and bulk modulus, and viscosity. Due to uncertainties in measuring the flow-related parameters of permeability, pore size and virtual mass, those parameters are treated as random variables. The inversion, tested on four experimental data sets, is unable to reliably converge on the measured acoustic properties. Modification of the Biot model, by either adding loose grains to the pore fluid or making porosity a function of pore pressure, results in a much higher fraction of successful conversions.

This paper presents a method for estimating the physical and acoustic properties of the sea bed using the Biot model and data acquired by a chirp sonar, a wide-band reflection profiler. The reflection data is processed to measure the reflection coefficient of the sediment–water interface and the change in attenuation with frequency for the uppermost sediment layer. The inversion method utilizes the two acoustic measurements and the Biot model to estimate the physical and acoustic properties of the sea bed. This remote acoustic method may be quite useful for estimating sediment properties when no core data are available and the upper layer of the sea bed is homogeneous.

## II. BACKGROUND

### A. Review of the Biot Theory of Sound Propagation in Saturated Sediments

Biot [7] develops a pair of coupled differential equations to describe acoustic wave propagation in an isotropic saturated porous medium with permeability  $\kappa$ , pore fluid viscosity  $\eta$ , bulk density  $\rho$ , and fluid density  $\rho_f$ .

$$\nabla^2(H\varepsilon - C\zeta) = \frac{\partial^2}{\partial t^2}(\rho\varepsilon - \rho_f\zeta) \quad (4)$$

$$\nabla^2(C\varepsilon - M\zeta) = \frac{\partial^2}{\partial t^2}(\rho_f\varepsilon - m\zeta) - \frac{F\eta}{\kappa} \frac{\partial \zeta}{\partial t} \quad (5)$$

where  $\zeta$  is the incremental volume of fluid that enters or leaves the frame and  $\varepsilon$  is volumetric strain of the frame. Stoll [8] develops the following expressions for the Biot moduli in terms of measurable sediment properties:

$$H = \frac{(K_r - K_b)^2}{D - K_b} + K_b + \frac{4}{3}\mu \quad (6)$$

$$C = \frac{K_r(K_r - K_b)}{D - K_b} \quad (7)$$

$$M = \frac{K_r^2}{D - K_b} \quad (8)$$

$$D = K_r \left( 1 + n \left( \frac{K_r}{K_f} - 1 \right) \right) \quad (9)$$

where  $K_r$  is the grain bulk modulus,  $K_f$  is the modulus of the pore fluid, and  $n$  is porosity. The frame bulk modulus

$$K_b = K_{br} + jK_{bi} = K_{br} \left( 1 + j \frac{\delta_b}{\pi} \right) \quad (10)$$

and the frame shear modulus

$$\mu = \mu_r + j\mu_i = \mu_r \left( 1 + j \frac{\delta_s}{\pi} \right) \quad (11)$$

are complex moduli to account for dissipation losses at grain contacts, and  $\delta_b$  and  $\delta_s$  are the bulk and shear log decrements, respectively. The parameter

$$m = \frac{c\rho_f}{n} \quad (12)$$

accounts for the phase of fluid flow with respect to the macroscopic pressure gradient. The structure factor  $c$ , or tortuosity, is equal to 1 for uniform pores that are parallel to the pressure gradient and is equal to 3 for randomly oriented pores.

The factor  $F$  is a viscosity correction to account for frequency-dependent viscous losses of the oscillating flow in the sediment pores. For the case of pores that are cylindrical ducts, the correction factor is given by [9]

$$F(\xi) = \frac{\frac{\xi}{4}T(\xi)}{1 - \frac{2}{j\xi}T(\xi)} \quad (13)$$

where

$$T(x) = \frac{ber'(x) - jbei'(x)}{ber(x) - jbei(x)} \quad (14)$$

and where  $ber$  and  $bei$  are real and imaginary parts of the Kelvin function,  $ber'$  and  $bei'$  are corresponding derivatives, and

$$\xi = a\sqrt{\frac{\omega\rho_f}{n}} \quad (15)$$

where the  $a$  is the pore radius. For pores other than circular ducts,  $a$  is called the pore-size parameter and is dependent on the shape and size of the sediment pores.

Stoll [8] develops the following expression for a harmonic plane wave traveling through a porous medium:

$$\begin{vmatrix} Hk^2 - \rho\omega^2 & \rho_f\omega^2 - Ck^2 \\ Ck^2 - \rho_f\omega^2 & m\omega^2 - Mk^2 - j\frac{\omega F\eta}{\kappa} \end{vmatrix} = 0. \quad (16)$$

The wavenumbers of the fast and slow wave are found by solving for  $k$  as

$$\begin{aligned} & (Hk^2 - \rho\omega^2) \left( m\omega^2 - Mk^2 - j\frac{\omega F\eta}{\kappa} \right) \\ & - (Ck^2 - \rho_f\omega^2)(\rho_f\omega^2 - Ck^2) = 0 \end{aligned} \quad (17)$$

$$\begin{aligned} & (-HM + C^2)k^4 \\ & + \left( Hm\omega^2 + \rho\omega^2 M - jH\frac{\omega F\eta}{\kappa} - C\rho_f\omega^2 - C\rho_f\omega^2 \right) k^2 \\ & - \rho m\omega^4 + j\frac{\rho F\eta\omega^3}{\kappa} + \rho_f\omega^4 = 0. \end{aligned} \quad (18)$$

Note that (18) is a quadratic expression in terms of  $k^2$

$$a(k^2)^2 + bk^2 + c = 0. \quad (19)$$

Therefore, the solution has the form

$$k^2 = \frac{-b \pm \sqrt{b^2 - 4ac}}{2a} \quad (20)$$

where the  $+$  sign provides  $k^2$  for the fast wave and the  $-$  sign provides  $k^2$  for the slow wave and where

$$a = C^2 - HM \quad (21)$$

$$b = Hm\omega^2 + \rho\omega^2 M - jH\frac{\omega F\eta}{\kappa} - C\rho_f\omega^2 - C\rho_f\omega^2 \quad (22)$$

$$c = -\rho m\omega^4 + j\frac{\rho F\eta\omega^3}{\kappa} + \rho_f\omega^4. \quad (23)$$

The complex wavenumber can be written in the following form:

$$k = k_r - j\alpha \quad (24)$$

where

$$\alpha = \text{Im}\{k\} \quad (25)$$

is the attenuation [nepers/meter] and

$$k_r = \text{Re}\{k\} = \frac{\omega}{V} \quad (26)$$

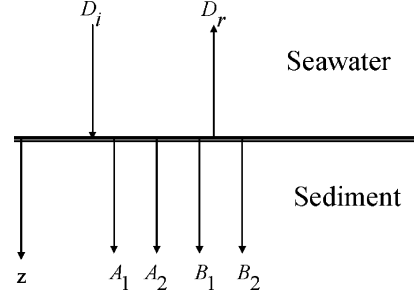


Fig. 1. Geometry for developing an expression for the reflection coefficient in terms of Biot parameters. The complex displacement amplitudes of the incident and reflected water waves are  $D_i$  and  $D_r$ , respectively.  $A_1$  and  $A_2$  are the complex displacement amplitudes of the frame due to fast and slow waves, respectively.  $B_1$  and  $B_2$  are the complex relative displacements of the pore fluid moving with respect to the frame (fluid volume per unit area of sediment) due to the fast and slow waves, respectively.

where  $V$  is the phase velocity of the traveling wave. Equations (25) and (26) will be used to calculate the attenuation and phase velocity for the fast wave.

### B. Review of the Reflection Coefficient Calculation

Consider the geometry in Fig. 1, which consists of seawater and sediment half spaces where the sediment–water interface is at  $z = 0$ .

The reflection coefficient of the sea bed can be determined by applying the following boundary conditions to the solutions of the wave equations at the sediment–water interface [8]:

- 1) continuity of fluid displaced in and out of the skeletal frame in a direction normal to the interface;
- 2) equilibrium of total stress across the interface;
- 3) equilibrium of fluid pressure across the interface.

Applying the boundary conditions to the equations of motion yields the following set of equations [8]:

$$\frac{D_r}{D_i} + (G_1 - 1)\frac{A_1}{D_i} + (G_2 - 1)\frac{A_2}{D_i} = -1 \quad (27)$$

$$\begin{aligned} \rho_w c_w \omega \frac{D_r}{D_i} + (Hk_1 - Ck_1 G_1) \frac{A_1}{D_i} \\ + (Hk_2 - Ck_2 G_2) \frac{A_2}{D_i} = \rho_w c_w \omega \end{aligned} \quad (28)$$

$$\begin{aligned} -\rho_w c_w \omega \frac{D_r}{D_i} + (Mk_1 G_1 - Ck_1) \frac{A_1}{D_i} \\ + (Mk_2 G_2 - Ck_2) \frac{A_2}{D_i} = \rho_w c_w \omega \end{aligned} \quad (29)$$

where

$$G_1 \equiv \frac{B_1}{A_1} = \frac{Hk_1^2 - \rho\omega^2}{Ck_1^2 - \rho_f\omega^2} \quad (30)$$

$$G_2 \equiv \frac{B_2}{A_2} = \frac{\rho\omega^2 - Hk_2^2}{\rho_f\omega^2 - Ck_2^2}. \quad (31)$$

In these expressions,  $\rho_w$  and  $c_w$  are the bulk density and sound speed for seawater, respectively, and  $k_1$  and  $k_2$  are the wavenumbers for the fast and slow waves, respectively.

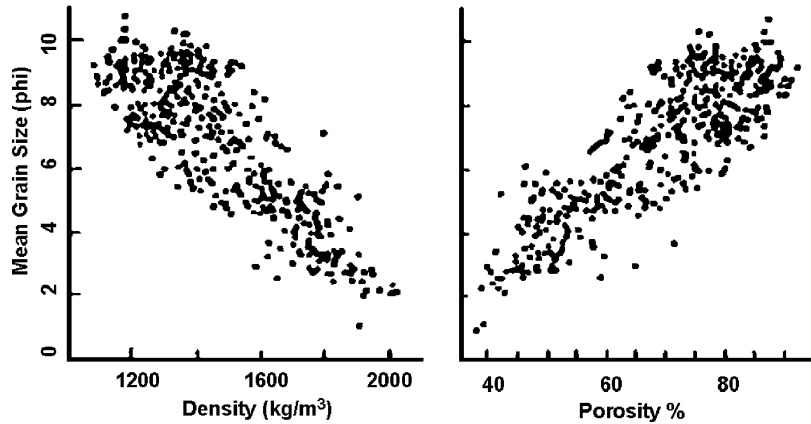


Fig. 2. Mean grain size  $\phi$  versus bulk density and porosity for sediment samples from the abyssal plain, abyssal hill, and continental shelf and slope [10].

The solution to (27)–(29) yields  $D_r/D_i$ , the ratio of the displacement amplitudes of the incident and reflected waves. The displacement amplitude ratio is identical to the pressure reflection coefficient of the sediment–water interface

$$R = \frac{D_r}{D_i}. \quad (32)$$

### III. APPROACH

#### A. Development of an Inversion Method

The proposed inversion method is based on the observation that field data [1] and Biot theory analyses [6] show that the reflection coefficient of the sea bed is strongly correlated with bulk sediment properties and is weakly related to permeability and grain size. Based on this observation, the porosity of the sea bed will be estimated using the reflection coefficient.

In some circumstances, porosity is independent of grain size. Fig. 2 contains a plot of mean grain size against porosity, showing that a sediment of a given grain size can have a wide range of porosities. If a sediment sample consists of uniform-diameter grains, different grain-packing configurations result in different porosities [10]. For example, the porosity of an ideal sand consisting of spherical particles with uniform diameter depends only on the packing and not on the diameter of the spheres. The ideal sand has a maximum porosity of 0.476 for simple cubic packing and a minimum porosity of 0.26 for dense packing; those porosities are independent of grain size [11]. In marine sediments, porosity is also affected by the particle-size distribution and the shape of the grains, which result in a weak correlation between porosity and grain size. In general, porosity increases with smaller particle sizes, with more uniform grain sizes, and with greater angularity of the grains. Table I provides the range of porosities for natural beds of marine sands [12].

Bachman [10] provides the following regression equation and standard error for porosity and mean grain-size data collected in all environments: the continental shelf and slope, and abyssal hill and plain.

$$n = 0.208 + 0.0943\phi - 0.00334\phi^2, \quad \sigma_n = 0.066. \quad (33)$$

TABLE I  
POROSITY OF NATURAL SAND BEDS [11]

	Well-sorted	Average	Well-mixed
Loosely-packed	0.46	0.43	0.38
Average	0.42	0.4	0.33
Densely-packed	0.4	0.37	0.3

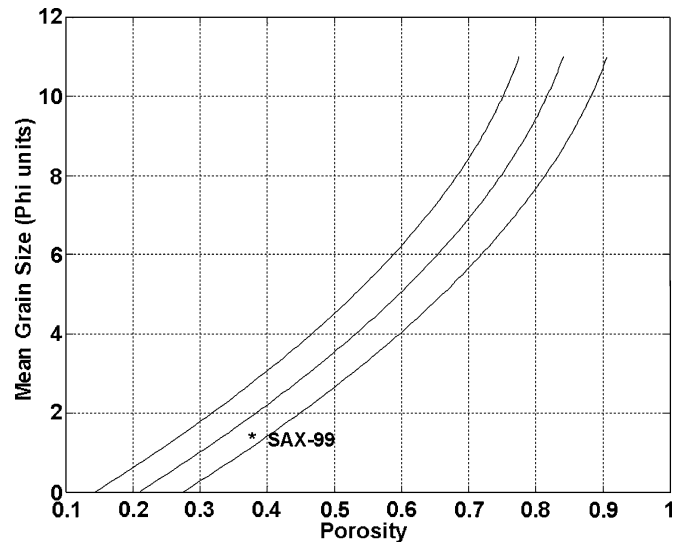


Fig. 3. Expected mean grain size plotted against porosity showing the 70% confidence limits of equation (33). The datum  $1.32\phi$ ,  $n = 0.372$  represents the average values of mean grain size and porosity of surficial sediments (top 13 cm) measured at the SAX-99 site off Fort Walton Beach, FL [13].

Solve (33) for  $\phi$  to obtain

$$\phi = \frac{0.0943 - \sqrt{0.0943^2 - 4(0.0034)(n - 0.208)}}{2(0.0034)} \quad (34)$$

where  $\phi$ , the mean grain size, in phi units, is related to the mean grain diameter  $d_{\text{mm}}$  (millimeter units) by

$$\phi = -\log_2 d_{\text{mm}}. \quad (35)$$

The mean grain size–porosity regression (33) and the standard error envelope are plotted in Fig. 3 to show the region of mean grain size and porosity measurements associated with approximately 70% of all sediment samples. The standard error for

TABLE II  
WENTWORTH SCALE FOR CLASSIFYING SEDIMENTS  
BASED ON MEAN GRAIN SIZE [14]

Sediment size description	Grain diameter (phi units)
Cobbles and boulders	Less than -6
Very coarse pebbles	-6 to -5
Coarse pebbles	-5 to -4
Medium pebbles	-4 to -3
Fine pebbles	-3 to -2
Very fine pebbles	-2 to -1
Very coarse sand	-1 to 0
Coarse sand	0 to 1
Medium sand	1 to 2
Fine sand	2 to 3
Very fine sand	3 to 4
Coarse silt	4 to 5
Medium silt	5 to 6
Fine silt	6 to 7
Very fine silt	7 to 8
Clay	Greater than 8

porosity may change with grain size, as seen in Fig. 2. The following analyses assume that the standard error is independent of grain size. Equation (33) will be used to calculate the “expected porosity” from the mean grain size. Given the porosity, the “expected mean grain size” will be calculated using (34). Note that the standard deviation of the expected mean grain size increases with increasing porosity, as shown in Fig. 3.

The Wentworth scale (Table II) provides the relationship between mean grain size (in phi and millimeter units) and sediment type. The proposed inversion procedure predicts the mean grain size of the top sediment layer. After the grain size is determined, the Wentworth scale is used to look up the sediment type.

The inversion method proposed in this paper uses the measured reflection coefficient to predict bulk sediment properties, such as porosity and density, and uses the porosity estimate and the measured attenuation rolloff to determine permeability and mean grain size. Since the Biot model requires 13 inputs to calculate the reflection coefficient and attenuation functions, interrelationships between inputs are needed to reduce the complexity of the analysis.

The first step of the inversion procedure is to estimate the porosity of the surficial sediment layer using the reflection coefficient. The relationship between the reflection coefficient and porosity (32) is generated by varying porosity from 0.25 to 0.8, by calculating the mean grain diameter using (34) for each porosity value, and by using property inter-relationships to calculate the remaining inputs of the Biot model. Table III provides the values or interrelationships used to generate the Biot model input parameters which vary with porosity and mean grain diameter.

### B. Discussion of Table III: Biot Model Input Parameters

The values of fluid density, bulk modulus, and viscosity are estimated from water temperature and salinity measurements. Grain density and bulk modulus values are based on the mineralogy of the sediments in the region. The values of the six properties for the SAX-99 site [4], which is the site used to test the inversion procedure, are given in Table III. These six properties

and the measurements of the reflection coefficient and attenuation rolloff are the inputs to the proposed inversion procedure.

1) *Permeability*: Some investigators using the Biot model to estimate acoustic sediment properties from physical properties select a hydraulic radius model for calculating permeability from mean grain diameter. For example, Hovem and Ingram [15] use the Kozeny–Carman equation

$$\kappa = \frac{d^2 n^3}{36K(1-n)^2} \quad (36)$$

to calculate the permeability of sand with porosity  $n$  and mean grain diameter  $d$ .

The coefficient  $K$  is 2 for circular tubes and 5 for spherical grains. Permeability measurements on sands and glass beads show that (36) and  $K = 5$  provide permeability estimates with less than a 50% error except for Panama City sands. Equation (36) overestimates the permeability of Panama City sands by about 2.5 [15].

Holland [3] uses another form of the Kozeny–Carman equation, given by [16]

$$\kappa = \frac{n^3}{K S_0^2 (1-n)^2} \quad (37)$$

to estimate permeability from the grain-size distributions for samples of silty clay and sand. The effective surface area of spherical grains is given by

$$S_0 = \sum_n \frac{6f_n}{d_n} \quad (38)$$

where  $f_n$  is the volume fraction of grains with diameter  $d_n$ .

The Kozeny–Carman equation (36) significantly overestimates the permeability of the well-sorted medium sands at the SAX-99 site off Fort Walton Beach. Given that the average porosity and mean grain size of the sands at the SAX-99 site is 0.372 and 1.32  $\phi$ , respectively [13], the Kozeny–Carman equation (36) yields a permeability of  $1.24 \times 10^{-10}$  m<sup>2</sup>. The sediment permeability measured with a constant head permeameter is  $3.3 \times 10^{-11} \pm 0.6 \times 10^{-11}$  m<sup>2</sup> [13]. The reason for this error is that the Kozeny–Carman equation, which is based on the hydraulic radius model, attempts to equate flow through parallel tubes with that of flow through granular materials by equating their hydraulic radii, which by definition is twice the volume of the voids divided by the surface area of the channel wall. The Kozeny–Carman equation is accurate only for specific cases such as unconsolidated well-sorted sediments with rounded grains [17], [18].

Accurate calculation of permeability for consolidated or poorly sorted sediments requires characterization of the pore geometry. The permeability of sediments is controlled by the geometry of the pore network that lies between the sediment grains. Juang [19], [20], Childs [21], Garcia-Bengochea [22], and Marshall [23] describe models and experiments that use pore-size distribution measurements to accurately estimate sediment permeability for a wide range of grain sizes and pore-size distributions functions. There is no simple relationship between the pore-size distribution and the grain-size distribution because

TABLE III  
PARAMETERS AND PROPERTY INTERRELATIONSHIPS USED TO GENERATE INPUTS FOR THE BIOT MODEL

Input parameter	Units	Parameter value or relationship	Reference
Porosity $n$	Fractional	0.25 to 0.8	
Fluid density	Kg/m <sup>3</sup>	1023	Williams[4]
Fluid bulk modulus	Pa	2.395x10 <sup>9</sup>	Williams[4]
$K_f$			
Grain density $\rho_g$	Kg/m <sup>3</sup>	2690	Williams[4]
Grain bulk modulus	Pa	3.2x10 <sup>10</sup>	Williams[4]
$K_y$			
Absolute Viscosity $\eta$	Kg/m-s	0.001	Williams[4]
Permeability $\kappa$	m <sup>2</sup>	$\kappa = \frac{d^2 n^3}{180(1-n)^2} \frac{1}{\sqrt{10}}$	See notes for table
Pore size $a$	m	$a = \frac{d}{3} \frac{n}{(1-n)} \frac{1}{1.8}$	See notes for table
Tortuosity $c$		$c = \begin{cases} 1.35 & \phi \leq 4 \\ -0.3 + 0.4125\phi & 4 < \phi < 8 \\ 3.0 & \phi \geq 8 \end{cases}$	See notes for table
Frame shear modulus	Pa	$\mu_r = 1.835 \times 10^5 e^{-1.12 \sqrt{r_a(z)}}$	Yamamoto[27]
$\mu_r$			
Shear log decrement		$\delta_s(z_0) = \delta_s(z_0) \sqrt{z_0/z}$	Stoll[8]
$\delta_s$			
Frame bulk modulus	Pa	$K_{br} = \frac{2\mu_r(1+\sigma)}{3(1-2\sigma)}$	Ogushwitz[28]
$K_{br}$			
Bulk log decrement $\delta_f$		$\delta_f(z_s) = \delta_f(z_0) \sqrt{z_0/z_s}$	Stoll[8]

the pore geometry is influenced by factors other than grain size, such as consolidation and sediment fabric (e.g., aggregation of similar size grains, particle orientation, and grain shape). Those unknown factors prevent developing an accurate relationship between mean grain size and permeability. Consequently, the Kozeny–Carman relationship will be used to estimate grain size from permeability and porosity estimates.

The error introduced by the Kozeny–Carman equation (36) in calculating permeability is established by studying published permeability measurement data. Based on 27 measurements of the top 10 cm of sandy sediment in the Southern Baltic Sea, Forester *et al.* [24] reported that the Kozeny–Carman relationship (36) overestimated permeability by an order of magnitude. Comparisons between measured and calculated permeability for 12 cores of intertidal sand flats in the North Sea show that (36) overestimates permeability by a factor of  $5.1 \pm 3.4$  [25]. Permeability measurements show that the Kozeny–Carman equation (36) is accurate for well-sorted unconsolidated sediments with rounded grains [15]. Consequently, the reported errors of the sediment properties predicted by the proposed inversion method will be based on the assumption that the Kozeny–Carman equation overestimates the permeability of sediments on the average by a factor of  $\sqrt{10}$  with error limits at overestimation factors of 1 and 10.

2) *Pore Size*: Hovem [15] uses the following expression developed using the hydraulic radius concept for uniform spherical grains to calculate the pore radius (or pore parameter):

$$a = \frac{d}{3} \frac{n}{(1-n)}. \quad (39)$$

The proposed inversion procedure assumes that the permeability of sediments is proportional to the square of the pore radius [21], [22]. From the discussion on permeability error, it follows that (39) overestimates the pore radius on the average by a factor of  $\sqrt[4]{10} = 1.8$  with overestimation factor limits of 1 and  $\sqrt{10}$ . Note that this assumption may not be accurate for fine-grained sediments that have a large component of plate-like clay particles.

Given that the pore geometry determines sediment permeability, the standard deviation of the pore-size distribution is expected to influence permeability. Yamamoto [26] uses a parallel tube model with a log-normal pore-size distribution to show that the standard error of the pore-size distribution has a significant effect on the permeability, the viscosity correction factor, and the attenuation coefficient of sediments. The permeability for the parallel tube model is given by

$$\kappa = \frac{n}{8} \int_0^{\infty} r^2 f(r) dr \quad (40)$$

where  $r$  is the pore radius and  $f(r)$  is the pore radius density function. Equation (40) shows that pore water flow through large pores dominates the permeability. Models that account for the fact that sediment pores are interconnected and that flow along any path is limited by the smallest pore size provide more accurate estimates of permeability than the parallel tube and hydraulic radius models. Pore distribution functions with a wide range of shapes are measured to show that interconnected pore models provide good estimates of sediment permeability [19],

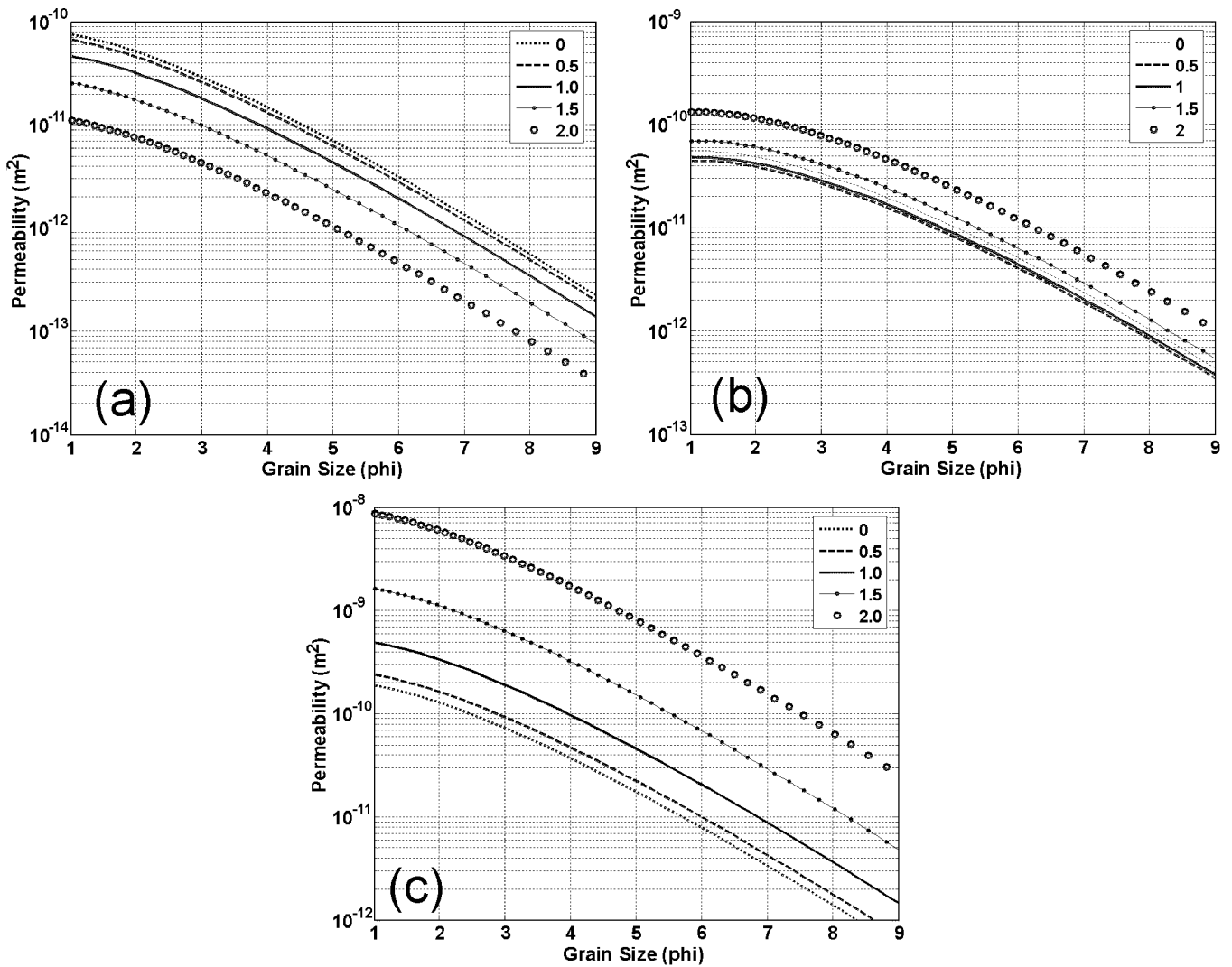


Fig. 4. Estimates of permeability from porosity and grain size for the following models. (a) Kozeny–Carman equation. (b) Interconnected pore model. (c) Parallel tube model. Permeability is plotted for log-normal pore- and grain-size distributions for five values of standard deviation: 0, 0.5, 1.0, 1.5, 2.0 $\phi$ .

[20], [22], [23]. One interconnected pore model is described by the expression

$$\kappa = \frac{n^2}{8} \int_0^\infty \int_0^\infty \hat{r}^2 f(r_i) f(r_j) dr_i dr_j \quad (41)$$

where  $\hat{r}$  is the smaller of the radii  $r_i$  and  $r_j$  of the connected ducts and accounts for flow through a sequence of two ducts being limited by the duct with the smallest diameter [22]. Permeability experiments show that the performance of the interconnected pore model (41) improves if a weighting factor is added to the integrand to account for tortuosity and the correlation between interconnected pore sizes caused by clustering of particle with similar sizes [19], [20], [22].

Under certain conditions, the Kozeny–Carman equation and the interconnected pore model (41) provide permeability estimates of the same order while the parallel tube model overestimates permeability by an order of magnitude. Fig. 4 is a comparison of permeability—grain-size curves calculated using the

Kozeny–Carman equation (37), the parallel tube model (40), and interconnected pore model (41) for various pore- and grain-size standard deviations. The expected porosity—mean grain size relation shown in Fig. 3—is used in the permeability calculations. Fig. 4(a) is based on a log normal grain-size distribution while Fig. 4(b) and 4(c) are based on  $f(r)$  having a log normal distribution. The relationship between the pore radius and grain diameter used to calculate the pore model curves in Fig. 4(b) and 4(c) is given by (40). The comparison shows that the Kozeny–Carman hydraulic radius model and the interconnected pore model predict permeabilities of the same order of magnitude. Note that the interconnected pore model produces a permeability that is less sensitive to the standard deviation of the pore-size distribution. For pore-size standard deviations greater than  $1\phi$ , the parallel tube model overestimates permeabilities by at least an order of magnitude over the experimentally supported interconnected pore model. Fig. 4(c) shows that as the pore-size standard distribution increases, the parallel tube model produces a rapid increase in permeability due to large particle sizes dominating the integrand of (40). Given that the parallel tube model

TABLE IV  
COMPARISON BETWEEN THREE MODELS FOR CALCULATING PERMEABILITY FROM THE GRAIN- AND PORE-SIZE DISTRIBUTIONS OF OTTAWA SAND AND THE MEASURED PERMEABILITY OF OTTAWA SAND [19]

Standard Deviation [ $\phi$ ]	Interconnected Model Permeability [m <sup>2</sup> ]	Parallel Tube Model Permeability [m <sup>2</sup> ]	Kozeny-Carman Permeability [m <sup>2</sup> ]	Measured Permeability [m <sup>2</sup> ]
0	1.3e-10	4.1e-10	1.1e-10	
0.5	1.0e-10	5.1e-10	1.0e-10	2.5e-11
1	1.1e-10	1.1e-9	6.9e-11	
2	3.1e-10	1.9e-8	1.6e-11	

does not appear to model pore-water flow accurately in ocean sediments, the relationships between the pore-size standard deviation, permeability, and attenuation based on the parallel tube model and described in [26] are not incorporated in the proposed inversion procedure.

Applying the three models to analyze Ottawa, ON, Canada, sand provides a specific example of their relative performance in predicting permeability from grain- or pore-size measurements. Ottawa sand described in [19] has an approximate log-normal grain-size distribution with a mean of 0.52 mm and a standard deviation of  $0.5\phi$ , a porosity of 0.324 (low compaction effort), and a pore-size distribution that is approximately log-normal with a standard deviation of  $0.5\phi$  and a mean pore radius of 100  $\mu\text{m}$  measured by mercury intrusion porosimetry. For these porosity and mean grain diameter values, the pore radius calculated using (39) is about 83  $\mu\text{m}$ , which is 17% below the measured mean pore radius of 100  $\mu\text{m}$ , but falls within the error range of (39).

Table IV contains the permeabilities produced by the three models using the measured porosity, mean grain, and pore sizes for Ottawa sand with log-normal pore- and grain-size distributions. The standard deviations of the distributions are varied above and below the measured value of  $0.5\phi$  to show its effect on permeability for the three models. Note for the case of  $0.5\phi$ , the measured standard deviation for Ottawa sand, that the interconnected pore and the Kozeny–Carman (37) models provide the same permeability while the parallel tube model produces a permeability that is higher by a factor of 5. This discrepancy is greater for grain- and pore-size distributions with larger standard deviations. As noted earlier, Juang [19] uses a weighting factor in the integrand of (41) to correct the interconnected pore permeability for tortuosity and particle aggregation to produce a more accurate estimate of measured permeability for Ottawa sand. The interconnected pore model shows that permeability is relatively insensitive to changes in the standard deviation of the pore diameter for sediments with log-normal pore distribution, except for very poorly sorted sediments. For very poorly sorted sediments, the interconnected model (41) predicts that permeability increases with the standard deviation of the pore-size distribution as the conductance of the large pores starts to dominate over the flow restrictions caused by the small pores.

3) *Tortuosity*: The structure constant, or tortuosity, is the square of the ratio of the minimum path length of a path through the pores to the straight path length. The structure constant  $c$  is equal to 1 for uniform pores, which are parallel to the pressure gradient and is equal to 3 for randomly oriented pores [8].

Williams concludes that a tortuosity of 1.35 provides a best fit for sound-speed and attenuation data collected at the SAX-99 site [4]. Tortuosities will increase as sediment grains become more flake-like. It is assumed that the tortuosity reaches an upper limit of 3.0 for clays due to the flake-like shape of the clay particles.

4) *Shear Modulus*: Yamamoto [27] plots the ratio of the shear modulus to the square root of the effective stress against the void ratio using published experimental data to obtain

$$\mu_r = 1.835 \times 10^5 e^{-1.12} \sqrt{\tau_a(z_s)} \quad (42)$$

where the void ratio  $e$ , which is the volume of the voids divided by the volume of the solids, is related to porosity by

$$e = \frac{n}{1-n}. \quad (43)$$

The average total stress  $\tau_a(z_s)$  at depth  $z_s$  is given by

$$\tau_a = \frac{1}{3}(\tau_x + \tau_y + \tau_z) \quad (44)$$

$$\begin{aligned} \tau_x &= K_0 \tau_z \\ \tau_y &= K_0 \tau_z. \end{aligned} \quad (45)$$

The effective stress  $\tau_z$  is the stress due to the sediment overburden, the total stress minus the pore pressure, and, for homogeneous sediments, is given by

$$\tau_z = (1-n)(\rho_g - \rho_f)gz \quad (46)$$

where  $g = 9.8 \text{ m/s}^2$  is the gravitational acceleration and  $z$  is the depth beneath the sea bed. The coefficient of earth pressure  $K_0$  is 0.5 based on an average of several hundred sediment cores collected on the continental shelf of the eastern United States [27].

5) *Frame Bulk Modulus*: The relationship for calculating the real part of the frame bulk modulus is given by

$$K_{br} = \frac{2\mu_r(1+\sigma)}{3(1-2\sigma)} \quad (47)$$

where  $\sigma$  is the dynamic Poisson's ratio of the sediment frame [28]. According to Stoll [29],  $\sigma$  falls within the range of

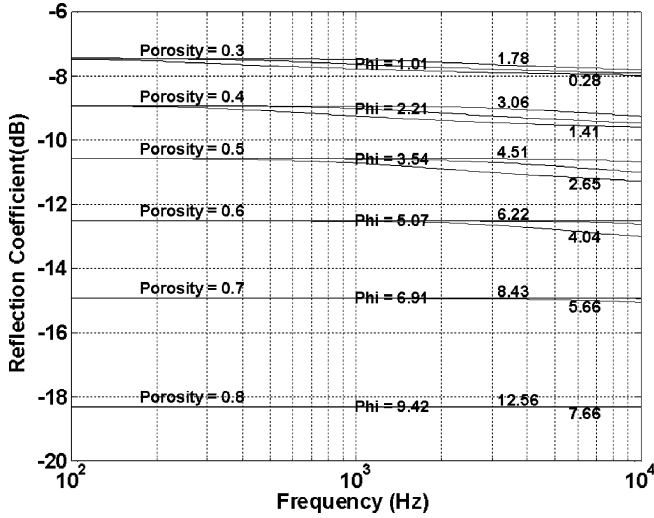


Fig. 5. Reflection coefficient function of frequency for six values of porosity. For each value of porosity, the reflection coefficient function is plotted for the expected mean grain size and for the 70% confidence intervals. The expected grain size introduces only a small error into the estimation of porosity from the reflection coefficient for most surficial sediments.

0.1–0.17 for sediments based on measurements of shear and dilatational wave velocities. Yamamoto [27] states that Poisson's ratio is in the range of 0.15–0.35 for unconsolidated marine sediments. This paper assumes that the relationship between Poisson's ratio and grain size is

$$\sigma = \begin{cases} 0.15 & \phi \leq 4 \\ -0.05 + 0.05\phi & 4 < \phi < 8 \\ 0.35 & \phi \geq 8 \end{cases}. \quad (48)$$

6) *Log Decrements*: The shear and dilatational log decrements for the sediment frame are inversely proportional to the effective stress [8]

$$\delta(z) = \delta(z_0) \sqrt{\frac{\tau_a(z_0)}{\tau_a(z)}} \quad (49)$$

where  $\tau_a(z)$  is the average total stress at depth  $z_s$ . Since the average total stress is proportional to subsurface depth for homogeneous sediments, the log decrement at a subsurface depth of  $z$  m is

$$\delta(z_s) = \delta(z_0) \sqrt{\frac{z_0}{z_s}}. \quad (50)$$

The values of the log decrement for volumetric and shear strain of the frame, determined by experiments conducted by Stoll [30], are approximately equivalent and equal to 0.1. The shear and log decrements are assumed to be 0.1 at a subsurface depth  $z_0$  of 20 cm (or, equivalently, 0.14 at 10 cm).

$$\begin{aligned} \delta_s(z_0 = 0.2 \text{ m}) &= 0.1 \\ \delta_f(z_0 = 0.2 \text{ m}) &= 0.1. \end{aligned} \quad (51)$$

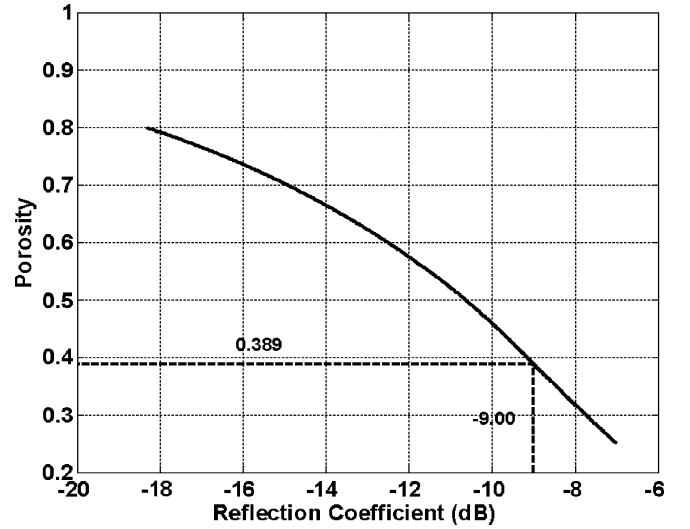


Fig. 6. Graph for estimating porosity from the reflection coefficient measurement at 2000 Hz. The bold line was calculated using the Biot model and the expected grain size (34). At the SAX-99 site, the reflection coefficient of  $-9.00$  dB at 2.0 kHz yields an estimated porosity of 0.389.

### C. Procedure for Estimating Porosity From the Reflection Coefficient

The inversion procedure estimates sediment porosity from the measured reflection coefficient using (32), the expected mean grain size (34), and the parameters in Table III. Fig. 5 shows that using the expected mean grain size to estimate permeability, a Biot model input parameter introduces only a small error in estimating porosity from the reflection coefficient for most sediments. The reflection coefficient is plotted as a function of frequency for six values of porosity. For each value of porosity, the reflection coefficient function is generated for the expected mean grain size and for the grain sizes associated with 70% confidence limits of (34).

The porosity of the sea bed is obtained from the porosity–reflection coefficient relation at a selected measurement frequency. For example, at the SAX-99 experiment site, the reflection coefficient of the sediment–water interface measured with the chirp sonar at 2.0 kHz is  $-9.00$  dB with 70% confidence limits at  $-9.00 \pm 0.12$  dB. A curve for looking up the porosity using the reflection coefficient measurements is given in Fig. 6. The reflection coefficient–porosity relation at 2.0 kHz was calculated using (32), the regression equation (34), and the property interrelationships in Table III. Porosity errors are determined by regenerating Fig. 6 for each of the 70% confidence limits of the measured reflection coefficient. The error limits of porosity associated with 70% confidence limits of the reflection coefficient measurement  $-9.00 \pm 0.12$  dB are  $0.389 \pm 0.08$ . A more detailed discussion of the porosity error is left for the Results section.

### D. Procedure for Estimating Grain Size From the Attenuation Rolloff Measurement

The procedure for estimating mean grain size consists of two main steps. The first step is to calculate the permeability given the attenuation rolloff measurement and porosity estimated from

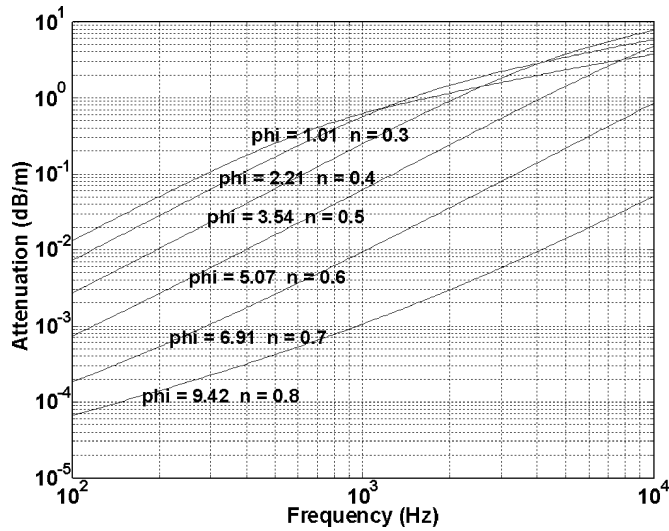


Fig. 7. Attenuation functions for six porosities and associated expected mean grain sizes for sediments from all environments. Note that slope of the attenuation function changes with frequency.

the reflection coefficient measurement. Then, the mean grain size is determined from the modified Kozeny–Carman equation given in Table III and the porosity and permeability estimates.

The attenuation rolloff is the change in attenuation with frequency measured over the operating band of the sonar and reported at the center frequency of the measurement. The attenuation rolloff is approximately equal to the slope of the attenuation versus frequency function. The attenuation rolloff will change with frequency because attenuation is not linearly dependent on frequency.

The attenuation of the fast wave (25) is plotted against frequency in Fig. 7 for various porosities in the range of 0.3–0.8 using the expected mean grain size to calculate the expected permeability of the modified Kozeny–Carman equation in Table III. The plot shows that the slope of the attenuation function varies with frequency. Assume that the frequency dependence of attenuation can be represented by

$$\beta = k' f^m \tag{52}$$

where  $\beta$  is attenuation (in decibels per meter),  $k'$  is the attenuation coefficient (in decibels per meter per hertz), and frequency  $f$  is in kilohertz. Take the logarithm of (52) to obtain

$$\log \beta = \log k' + m \log f. \tag{53}$$

Note that when  $m = 1$ , attenuation is proportional to frequency and the slope of the  $\log \beta$  versus  $\log f$  plot equals one. Fig. 7 shows that the attenuation is usually not linearly dependent on frequency according to Biot theory.

Using five values of permeability extending over the error range of the Kozeny–Carman relation, attenuation is plotted against frequency in Fig. 8 for  $n = 0.389$  and  $2.07\phi$ , the porosity and expected mean grain size determined from the reflection coefficient of  $-9.0$  dB. The center curve in Fig. 8 is based on the expected permeability of  $1.57 \times 10^{-11} \text{ m}^2$ . The other curves cover the one decade permeability error introduced by the Kozeny–Carman equation. This figure shows the large

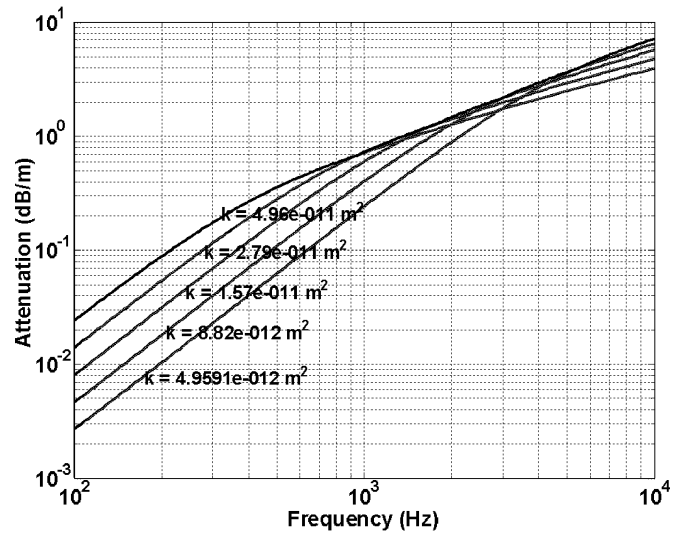


Fig. 8. Fast wave attenuation for the range of permeabilities expected for a sediment with a porosity of 0.389 and a mean grain size of  $2.07\phi$ .

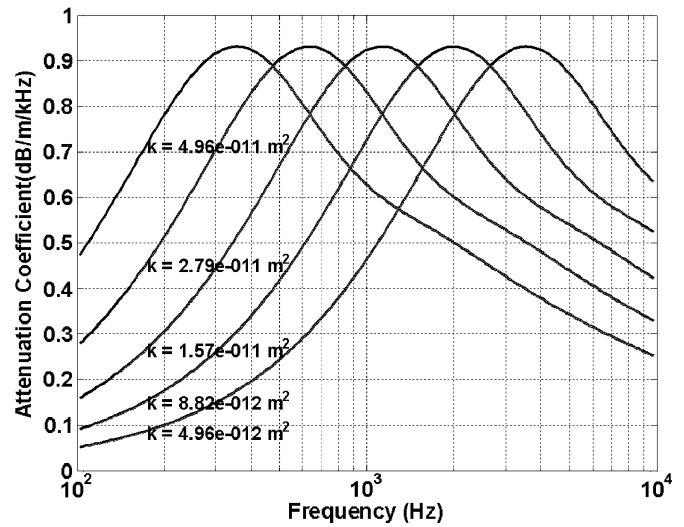


Fig. 9. Attenuation rolloff for the range of permeabilities expected for a sediment with a porosity of 0.389 and a mean grain size of  $2.07\phi$ . At the attenuation rolloff measurement frequency of 6 kHz, the permeability can be uniquely determined from the attenuation rolloff.

influence that permeability has on the fast wave attenuation of sediments.

The attenuation rolloff function, which is the slope of the attenuation function shown in Fig. 8, is plotted in Fig. 9. The plot demonstrates that the attenuation rolloff is sensitive to permeability and that the permeability provides a unique attenuation rolloff value for frequencies above 3.5 kHz and below 350 Hz for the range of permeabilities expected for a sediment with a porosity of 0.389 and a mean grain size of  $2.07\phi$ . To determine the permeability for a given attenuation rolloff, plot attenuation rolloff against permeability at the center frequency of the attenuation rolloff measurement and lookup the permeability.

After obtaining the permeability from the attenuation rolloff measurement, the porosity and permeabilities values are refined by reiterating the above procedure. The updated value for permeability is used to recalculate the reflection coefficient–porosity curve, to obtain a better estimate of porosity.

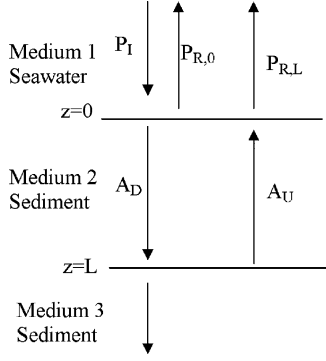


Fig. 10. Geometry for the discussion on estimating the slope of the attenuation function from the attenuation rolloff measurement.

The updated porosity estimate is used to generate a new attenuation rolloff–permeability curve to obtain a better estimate of permeability and so on. Note that during the recursive procedure the Kozeny–Carman equation is not used to calculate permeability; it was only used to calculate the initial permeability of the recursion. After the recursive procedure produces a unique estimate of permeability and porosity, the modified Kozeny–Carman equation is used to calculate the mean grain-size estimate. After updating the Biot model input parameters in Table III, the fast wave attenuation and velocity functions of frequency are generated using (25) and (26).

#### E. Background on the Attenuation Rolloff Measurement

To show that the attenuation rolloff provides the slope of the attenuation function, consider the propagation of fast waves shown in Fig. 10. For simplicity, consider plane wave propagation (sonar data are corrected for spherical spreading). Let  $P_I$ ,  $P_{R,0}$ , and  $P_{R,L}$  be the amplitude spectra of the transmitted (or incident) pulse and the reflections from the sediment–water ( $z = 0$ ) and sediment–sediment interfaces ( $z = L$ ), respectively. Let  $A_D$  and  $A_U$  be the amplitude spectra of the downward and upward traveling fast waves in the sediment layer. The amplitude spectra of the fast waves traveling in the sediment layer are a function of distance traveled and are given by

$$A_D(z) = A_D(0)e^{-\alpha z} \quad (54)$$

$$A_U(z) = A_U(L)e^{-\alpha(L-z)} \quad (55)$$

where  $\alpha$  is the attenuation (decibel/neper). Let  $T_{12}$  and  $T_{21}$  be the pressure transmission coefficients for waves traveling from medium 1 to 2 and from medium 2 to 1, respectively. Let  $R_1$  and  $R_2$  be the reflection coefficients of the upper and lower interfaces. The coefficients are given by

$$T_{12} = \frac{A_D(0)}{P_I} \quad (56)$$

$$T_{21} = \frac{P_{R,L}}{A_U(0)} \quad (57)$$

$$R_1 = \frac{P_{R,0}}{P_I} \quad (58)$$

$$R_2 = \frac{A_U(L)}{A_D(L)}. \quad (59)$$

Given that the interface echoes are time gated, interlayer multiples are ignored. It follows that the measured amplitude spectrum for the wave reflected from the interface at the bottom of the sediment layer is given by

$$P_{R,L} = P_I T_{12} R_2 T_{21} e^{-2\alpha L}. \quad (60)$$

The measured amplitude spectrum of the sediment–water interface echo is given by

$$P_{R,0} = P_I R_1. \quad (61)$$

The first step of the attenuation rolloff measurement procedure is to calculate the spectral ratio or sediment transfer function given by

$$\begin{aligned} T(f) &= \frac{P_{R,L}}{P_{R,0}} = \frac{T_{12} R_2 T_{21}}{R_1} e^{-2\alpha L} \\ &= T_0 e^{-2\alpha L} = T_0 10^{-\frac{2\beta L}{20}} \end{aligned} \quad (62)$$

where  $T_0$  accounts for the transmission and reflection coefficients at the boundaries.

Note that the relationship between the attenuations  $\beta$  (in decibel per meter) and  $\alpha$  (in nepers per meter) can be shown by taking 20 times the logarithm of both sides of

$$e^{-2\alpha L} = 10^{-\frac{2\beta L}{20}} \quad (63)$$

to obtain

$$20\alpha \log e = \beta \quad (64)$$

$$8.686\alpha = \beta. \quad (65)$$

The relative attenuation  $\Lambda$  is defined as 20 times the logarithm of the transfer function divided by twice the layer thickness  $L$

$$\begin{aligned} \Lambda &= \frac{20 \log(T(f))}{2L} \\ &= \frac{20 \log\left(T_0 10^{-\frac{2\beta L}{20}}\right)}{2L} \\ &= \frac{20 \log T_0}{2L} - \beta. \end{aligned} \quad (66)$$

The attenuation rolloff is the slope of the relative attenuation function, which is given by

$$\frac{d\Lambda}{df} = \frac{d\left(\frac{20 \log T_0}{2L}\right)}{df} - \frac{d\beta}{df}. \quad (67)$$

For thick sediment layers and for transmission and reflection coefficients with weak frequency dependence

$$\frac{1}{2L} \frac{d(20 \log T_0)}{df} \ll \frac{d\beta}{df}. \quad (68)$$

It follows that the attenuation rolloff, which is the slope of the measured relative attenuation function, is approximately equal to the attenuation function of the Biot model

$$\frac{d\Lambda}{df} \cong -\frac{d\beta}{df}. \quad (69)$$

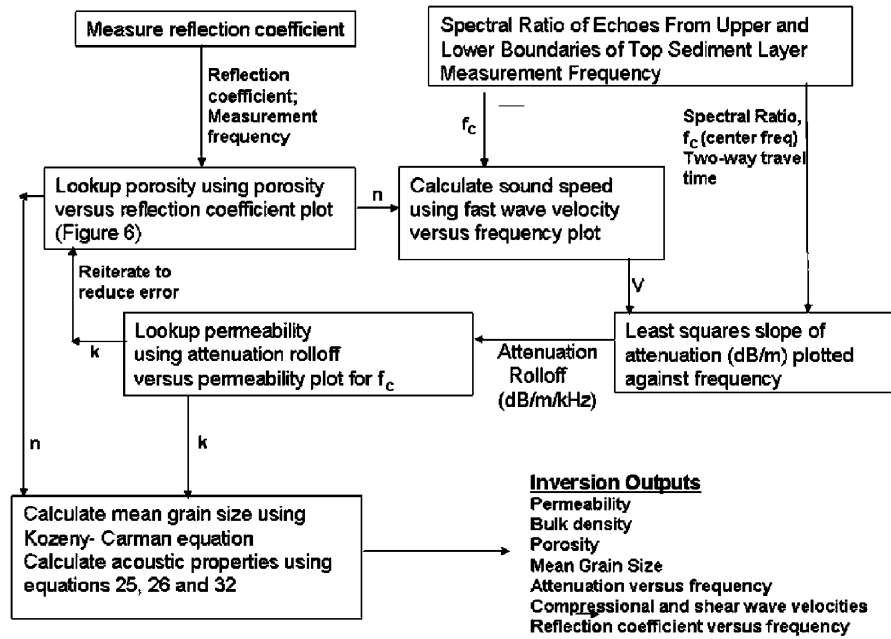


Fig. 11. Procedure for estimating the sediment properties of the top sediment layer using the reflection coefficient and attenuation rolloff measurements and the Biot model.

#### F. Summary of the Procedure for Remotely Estimating Sediment Properties Using Chirp Sonar Data

An overview of the procedure for remotely estimating the sediment properties of the upper sediment layer is given in Fig. 11. The absolute reflection coefficient of the sediment water interface is measured at normal incidence. The low end of the operating band is selected for measuring the reflection coefficient to ensure that the acoustic wavelength is much longer than the height of the bottom roughness and that the measurement averages over a large volume of sediment, thereby minimizing the effect of property gradients near the sediment–water interface.

The first step in the procedure is to estimate porosity from the reflection coefficient for a frequency near the low end of the sonar operating band. The porosity is obtained from a reflection coefficient–porosity plot generated using the expected grain size (32) and expected permeability of the modified Kozeny–Carman equation.

The next step is to measure the spectral ratio of the echoes from the upper and lower interfaces of the top sediment layer. This measurement is made over the widest possible frequency band so that the attenuation at the high end of the band is at least 20 dB greater than at the low end of the band. Meeting this criterion requires a large bandwidth (usually about two octaves) and a reflector with sufficient subsurface depth. This bandwidth criterion keeps errors associated with the frequency dependence of transmission and reflection coefficients, usually on the order of 1–2 dB, from causing more than a 10% error in estimating the attenuation rolloff. Reflector selection is critical for realizing accurate measurements of the attenuation rolloff. The reflector at the base of the top sediment layer must be flat and must be a step change in vertical impedance and not a scattering layer such as gassy or shell-filled sediments. An indicator of an irregular interface is the presence of notches or peaks in the spectral ratio.

The spectral ratio is divided by the two-way travel distance through the top sediment layer to generate a plot of attenuation versus frequency. The attenuation rolloff is the least-squares slope of a line fitted through the data points of the attenuation versus frequency plot. The two-way travel distance is based on echo arrival times and a sediment velocity calculated at the center frequency of the attenuation rolloff measurement using the estimated porosity and the expected permeability. The permeability is obtained from a plot of attenuation rolloff against permeability, generated for the center frequency of the spectral ratio measurement, and the porosity estimated from the reflection coefficient measurement. The tortuosity and Poisson’s ratio parameters used in this calculation are based on the expected grain size associated with the porosity estimate.

After reiterating the porosity and permeability calculations to converge on a solution based on the reflection coefficient and attenuation rolloff measurements, the resulting porosity and permeability values are used to calculate the mean grain size and the acoustic properties of the sediments. The output of the inversion provides the porosity, bulk density, permeability, fast and shear wave velocities and attenuation functions, and the reflection coefficient function.

#### IV. REMOTE ACOUSTIC MEASUREMENTS AT THE SAX-99 SITE

At the SAX-99 site, approximately 1 km offshore of Fort Walton Beach, FL, the chirp sonar was deployed in April 2002 to collect data to test the proposed inversion procedure. The sonar measured the reflection coefficient to be  $-9.00 \pm 0.12$  dB using a bandpass filter centered at 2 kHz with a  $-3$  dB bandwidth of 1000 Hz. More details on the chirp sonar system and the measurement of the reflection coefficient are provided in a companion paper in this journal issue [33]. The chirp sonar measured the average intensity of the sea-bed echo from 75 acoustic

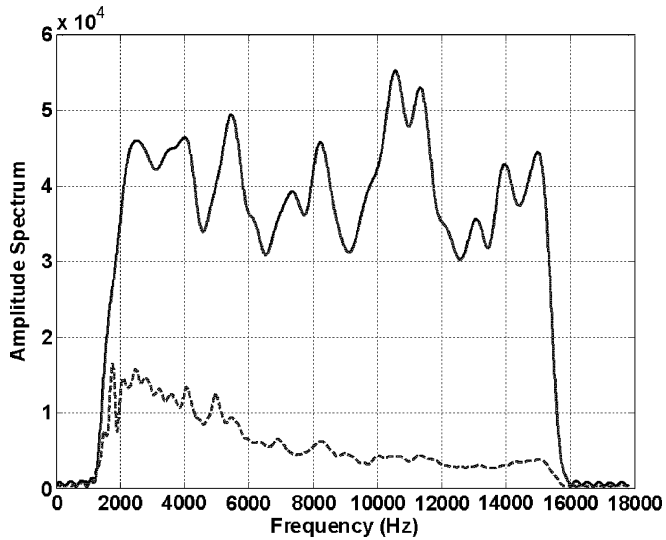


Fig. 12. Amplitude spectra of one air-water interface echo (collected at calibration site: solid line) and one sand-water interface echo (collected at SAX-99 site: dashed line).

returns while transiting 30 m over the SAX-99 APL tower site [31]. The reflection coefficient is calculated using

$$RL = 10 \log \left( \frac{\langle I_{\text{sea bed/water}} \rangle r_{\text{sea bed/water}}^2}{\langle I_{\text{air/water}} \rangle r_{\text{air/water}}^2} \right) \quad (70)$$

where  $\langle I_{\text{sea bed/water}} \rangle$  is the average intensity of the echo from the sea-bed-water interface and  $\langle I_{\text{air/water}} \rangle$  is the average intensity of the echo from a mirror-like air-water interface measured with the sonar vehicle inverted. The distances from the vehicle to the air-water and sediment-water interfaces are  $r_{\text{air/water}}$  and  $r_{\text{sea bed/water}}$ , respectively. The intensity of the echo from the air-water interface was measured with the chirp sonar inverted in a salt-water spring in southwestern Florida. The spring was over 100 ft wide and 100 ft deep and the water surface roughness was less than 1 cm during the calibration.

During the survey of the SAX-99 site, the chirp sonar transmitted FM pulses over the band of 1–15 kHz while the vehicle was being towed at an altitude of 3–6 m and at a speed of 1.5 m/s. Examples of the amplitude spectra for transmitted and reflected pulses are given in Fig. 12. For the reflection coefficient calculation, the echo intensities were measured at 2000 Hz using a pass-band filter with a bandwidth of 1000 Hz. The low end of the operating band was selected to minimize the effects of sea-bed surface scattering and vehicle motion. At the SAX-99 site, a laser line scan measured the heights of the sand ripples to be 4–6 cm peak to peak [31], which is much less than the acoustic wavelength at 2000 Hz. The projector and hydrophone arrays, used for the reflection measurements, are mounted adjacent to each other in a towed vehicle. The 8-in projector is practically omnidirectional at 2000 Hz. The sonar vehicle contains  $1 \times 1$  m and  $10 \times 10$  cm planar hydrophone arrays. The smaller hydrophone array is selected for the reflection coefficient calculation because the wide beamwidth of the array is desirable for minimizing the effect of vehicle motion on the reflection data.

The attenuation rolloff measurement requires the presence of a subsurface reflector for the spectral ratio calculation. However,

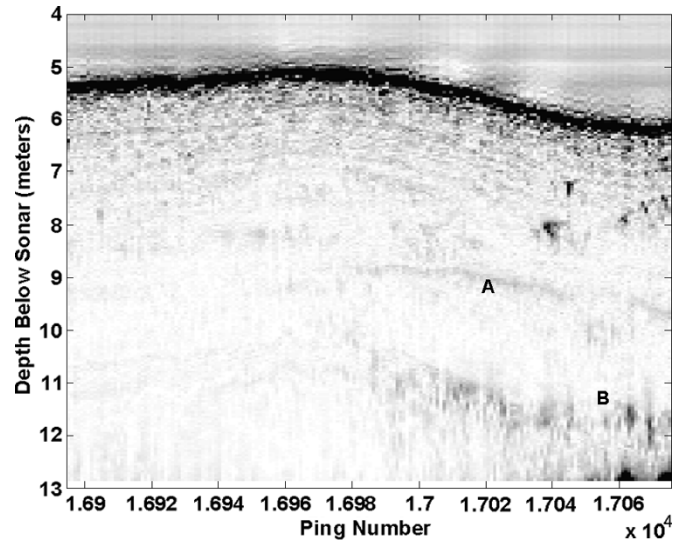


Fig. 13. Chirp sonar reflection profile at the SAX-99 site. The vertical scale is based on a water sound speed of 1530 m/s. Attenuation rolloff is measured using reflectors A and B.

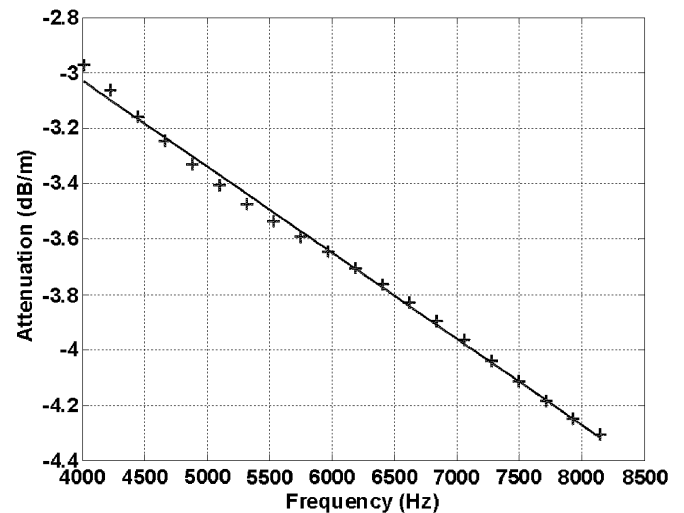


Fig. 14. Spectral ratio of echoes from the sediment-water interface and reflector A divided by the two-way path length. A line is fitted through the data by minimizing the square error. The slope of the line is 0.311 dB/m/kHz, the attenuation rolloff.

there are few subsurface reflectors within 100 m of the SAX-99 site off Fort Walton, Beach, FL; the site was selected for the sediment acoustic experiments because of its homogeneity. In the 2002 chirp sonar survey, a search was conducted in the vicinity of the SAX-99 site for subsurface reflectors with sufficient depth and with sufficient signal-to-noise ratio (SNR) (echo intensity to scattering noise intensity ratio) so that the spectral ratio could be measured over the band of 1–15 kHz. Vibracores in the vicinity of the SAX-99 site show that patches of mud are buried in the sandy sea bed. The subsurface reflections in the chirp sonar imagery are expected to be the result of those mud patches.

Chirp sonar images containing subsurface reflectors within 100 m of the SAX-99 APL tower site are shown in Fig. 13, 16, and 18. The images show reflectors labeled A, B, C, and D, which provide the subsurface echoes needed for the attenuation rolloff measurements. The reflection data were generated with

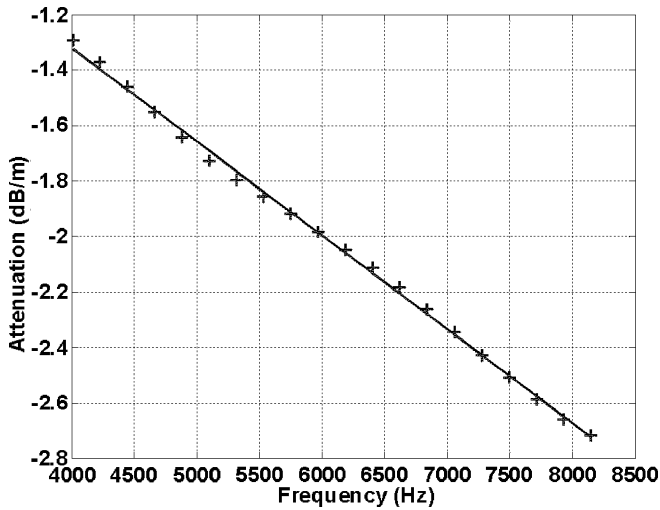


Fig. 15. Spectral ratio of echoes from the sediment–water interface and reflector B divided by the two-way path length. A line is fitted through the data by minimizing the square error. The slope of the line is 0.338 dB/m/kHz, the attenuation rolloff.

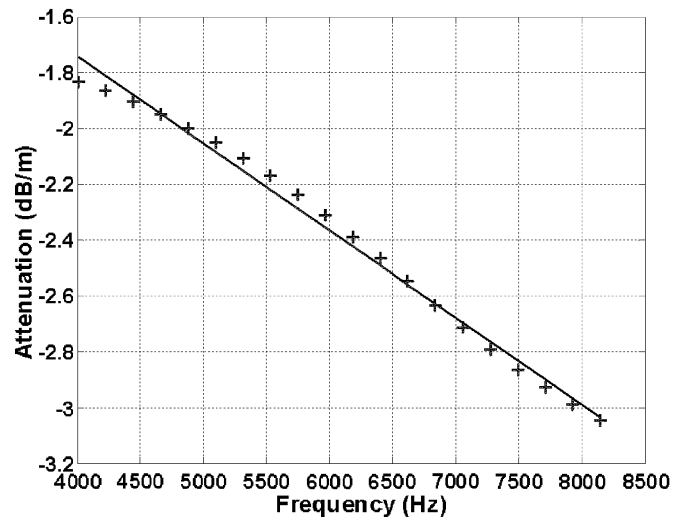


Fig. 17. Spectral ratio of echoes from the sediment–water interface and reflector C divided by the two-way path length. A line is fitted through the data by minimizing the square error. The slope of the line is 0.312 dB/m/kHz, the attenuation rolloff.

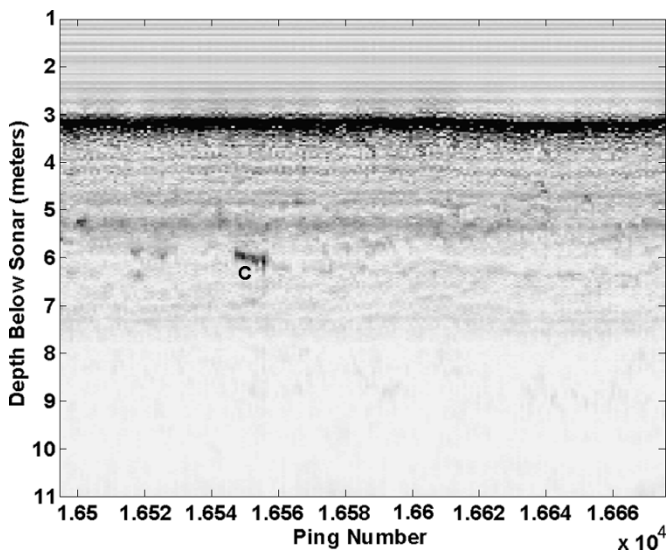


Fig. 16. Chirp sonar reflection profile at the SAX-99 site. The vertical scale is based on a water sound speed of 1530 m/s. Attenuation rolloff is measured using reflector C.

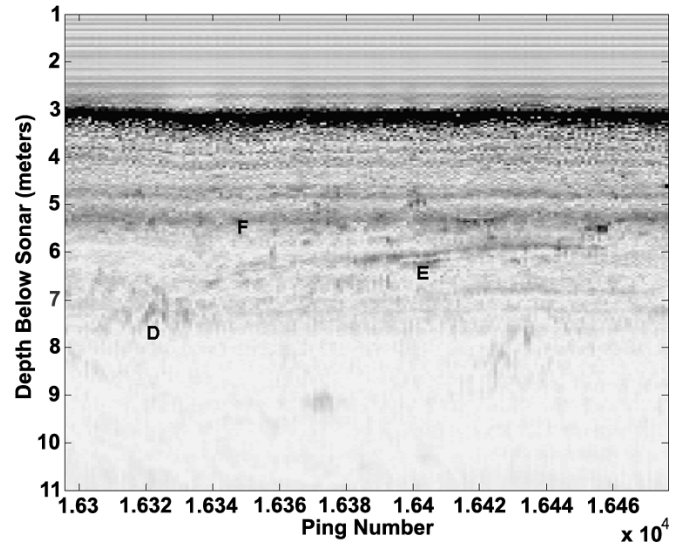


Fig. 18. Chirp sonar reflection profile at SAX-99 site. The vertical scale is based on a water sound speed of 1530 m/s. Attenuation rolloff is measured using reflector D. Reflectors E and F cannot be used for attenuation rolloff measurements, because the echoes contain interference caused by closely spaced reflectors (E) and a scattering layer (F).

a 10-ms-long FM pulse with a linear frequency sweep over the band of 1–15 kHz. Each subsurface image is constructed by stacking the envelopes of the matched-filtered acoustic returns.

Plots of the attenuation rolloff measurements follow each image. Each point in Fig. 14, 15, 17, 19, and 20 represents the spectral ratio of the echoes from the subsurface reflector and the sediment–water interface at the center frequency of a bandpass filter. The sonar data are filtered into 20 bands with a  $-3$  dB width of 2 kHz. This filter width is a tradeoff between measurement frequency resolution and SNR. As the filter width decreases, the frequency resolution improves, but the SNR degrades due to a reduction in temporal resolution and associated increase in the scattering noise contribution from sediments above and below the reflector. Each plotted point is the average amplitude of the filtered echoes from the

subsurface reflector divided by the average amplitude of the sediment–water interface echoes. This ratio is divided by the two-way path length of sound through the sediments above the selected layer interface.

Not all subsurface reflections are suitable for calculating the attenuation rolloff. If the impedance contrast at the bottom of the top sediment layer is not a step change in impedance, the echo from the contrast will contain interference. The vertical transition between the upper and lower sediment layers should be less than a tenth of a wavelength at the highest frequency of the attenuation rolloff measurement to prevent acoustic interference that causes peaks and notches in the echo spectrum. The image in Fig. 18 shows two examples of subsurface reflectors that generate echoes with significant acoustic interference. As

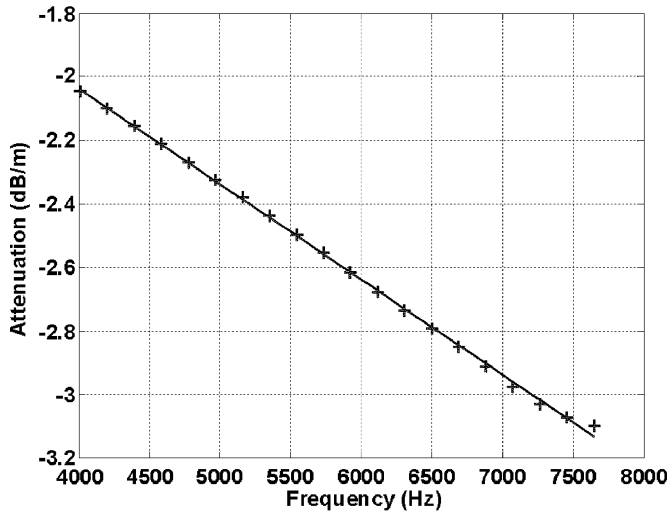


Fig. 19. Spectral ratio of echoes from the sediment–water interface and reflector D divided by the two-way path length. A line is fitted through the data by minimizing the square error. The slope of the line is 0.300 dB/m/kHz.

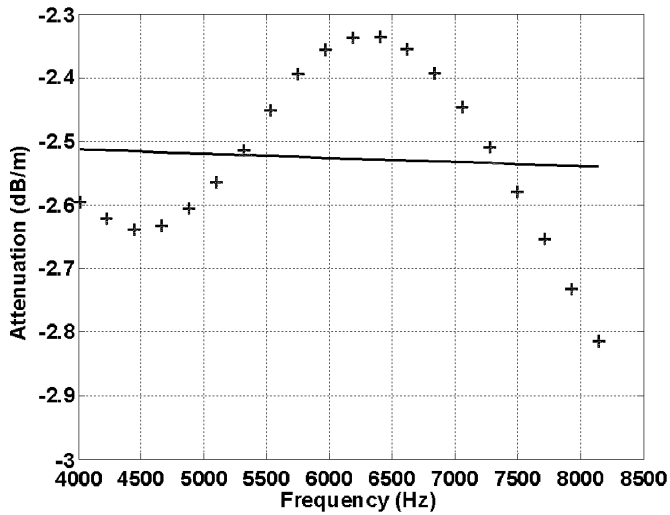


Fig. 20. Spectral ratio of the echoes from Reflector E and the sediment water interface contains interference from echoes originating at the top and bottom of the thin layer at reflector E shown in Fig. 18. Oscillations in the spectral ratio indicate interfering echoes.

shown in Fig. 20, the spectral ratio for reflector E has large oscillations caused by the double echo at reflector E, as seen in Fig. 18. Reflector F, which appears to be a scattering layer, also generates significant acoustic interference and is not usable for the attenuation rolloff measurement.

### V. RESULTS

Remote acoustic estimation of the acoustic and physical properties of the sea bed at the SAX-99 site is based on chirp sonar reflection coefficient and attenuation rolloff measurements. The reflection coefficient of the sediment–water interface measured at 2.0 kHz is  $-9.00$  dB with 70% confidence limits at  $-9.00 \pm 0.12$  dB. Recall that the reflection coefficient at 2.0 kHz was calculated using (32), the regression equation (34) relating porosity and expected mean grain size and the property interrelationships in Table III, and plotted

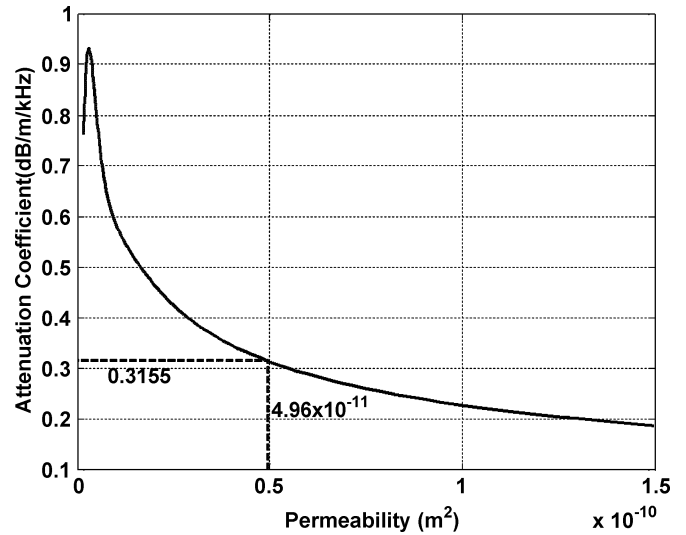


Fig. 21. Attenuation rolloff as a function of permeability at 6 kHz for sediments with a porosity of 0.389. The first iteration of the inversion predicts a permeability  $4.96 \times 10^{-11}$  m<sup>2</sup> for SAX-99 site sediments.

as a function of porosity in Fig. 6. In order to quantify the porosity errors, Fig. 6 is regenerated at the error limits of the reflection coefficient measurement. The 70% confidence limits of porosity associated with 70% confidence limits of the reflection coefficient measurement,  $-9.00 \pm 0.12$  dB are  $0.389 \pm 0.08$ . For the case of no reflection coefficient measurement error, the porosity error limits due to the one decade range of permeability error caused by the Kozeny–Carman equation are  $0.389 \pm 0.14$ . For the case of no reflection coefficient error and a correct expected permeability, the porosity error limits associated with the range of possible mean grain sizes for 70% of ocean sediments are  $0.389 \pm 0.13$ . If all three types of errors are considered, the porosity error limits are  $0.389 \pm 0.31$ . At the SAX-99 site, the average porosity measured using 18 diver cores is  $0.372 \pm 0.0073$  [13]. The permeability and mean grain size error limits associated with the porosity error limits are  $1.57 \pm 1.44 \times 10^{-11}$  m<sup>2</sup> and  $2.07 \pm 1.15\phi$ , respectively. Note that the permeability error limits are two decades apart. As shown later, the attenuation rolloff measurement significantly reduces the error for the estimated porosity, permeability, and mean grain size.

Given that the attenuation rolloff measurement is sensitive to permeability, the measurement provides a large reduction in the permeability error limits. The average attenuation rolloff for reflectors A, B, C, and D shown in Fig. 13, 16, and 18 is  $-0.3155$  dB/m/kHz. The center frequency of the measurement is 6 kHz. The porosity determined from the reflection coefficient measurement  $n = 0.389$  is used to generate the plot of attenuation rolloff against permeability shown in Fig. 21. From this plot, the permeability of the sediment is  $4.96 \times 10^{-11}$  m<sup>2</sup>. This permeability value is used to recalculate the reflection coefficient–porosity relationship and to obtain a new porosity value. After three cycles of this recursive procedure, the values of porosity and permeability converge to 0.376 and  $4.7 \times 10^{-11}$  m<sup>2</sup>, respectively. The error limits associated with the 50% confidence limits of the reflection coefficient measurement,  $-9.00 \pm 0.12$  dB are

TABLE V  
COMPARISON OF PHYSICAL SEDIMENT PROPERTIES PREDICTED  
FROM CHIRP SONAR DATA AND DIRECTLY MEASURED  
SEDIMENT PROPERTIES AT THE SAX-99 SITE

Sediment property	Predicted Properties (Based on reflection coefficient only)	Predicted Properties (3rd iteration of inversion of chirp sonar data)	Directly measured properties
Porosity	$0.389 \pm_{0.31}^{0.23}$	$0.376 \pm 0.007$	$0.372 \pm 0.0073$ [13]
Mean grain size (phi)	$2.07 \pm 1.15$	$1.18 \pm 0.94$	1.32 [13] 1.27 [32]
Sediment type	Fine sand	Medium Sand	Medium sand (Table II)
Permeability ( $10^{-11} \text{ m}^2$ )	$1.57 \pm_{1.44}^{15.5}$	$4.7 \pm_{0.8}^{0.2}$	Range of 0.3 to 6.1 [32] $3.6 \pm 0.7$ [13] Range of 1.8 to 5.1 [31]

$0.376 \pm 0.007$  and  $4.7 \times 10^{-11} \pm 0.2 \times 10^{-11} \text{ m}^2$  for porosity and permeability, respectively. The mean grain size obtained from the modified Kozeny–Carman equation, accounting for the equation's error and the reflection coefficient error, is  $1.18 \pm 0.85\phi$ . The attenuation rolloff measurements for the four reflectors varied from 0.300 to 0.338 dB/m/kHz. Executing the inversion for each of those limiting attenuation rolloff values provides error limits for porosity, permeability, and grain size of  $0.376 \pm 0.001$ ,  $4.7 \pm_{0.8}^{0.2} \times 10^{-11} \text{ m}^2$ , and  $1.18 \pm 0.94\phi$ , respectively. Therefore, the reflection coefficient measurement error is the major contributor to the porosity error while the attenuation rolloff measurement error is the largest source of error for the permeability estimate. The primary contributors to the mean grain-size error are the Kozeny–Carman equation and attenuation rolloff measurement errors.

A summary of comparisons between the physical sediment properties estimated from the inversion and direct measurements of those properties is given in Table V. The inversion procedure correctly predicted the porosity, mean grain size, and permeability of the sea bed within reported confidence limits of the direct measurements. The average porosity for all SAX-99 core sites is  $n = 0.372 \pm 0.0073(\pm\sigma)$  [13]. The mean grain size for the top 13 cm of sediments in 13 cores is  $1.32\phi$ . Both the directly measured mean grain size and the inversion-estimated mean grain size support the medium sand classification according the Wentworth scale given in Table II. Hydraulic conductivity measurements for the upper 13 cm of diver cores collected at the SAX-99 site have 70% confidence limits of  $3.6 \times 10^{-11} \pm 0.7 \times 10^{-11} \text{ m}^2$  [13]. The range of permeability measurements for the top 50 cm of SAX-99 sediments measured with an *in situ* permeability probe is  $0.3 - 6.1 \times 10^{-11} \text{ m}^2$  [32]. The error limits for the properties predicted by the inversion (third iteration) listed in Table V are based on the 70% confidence limits of the reflection coefficient measurement for the porosity estimate and the attenuation rolloff error range for grain-size and attenuation estimates. One potential problem with the validity of this comparison is that the inverted properties and directly measured properties are based on two different sediment volumes. The directly measurements were made on surficial sediments (primarily the top 13 cm)

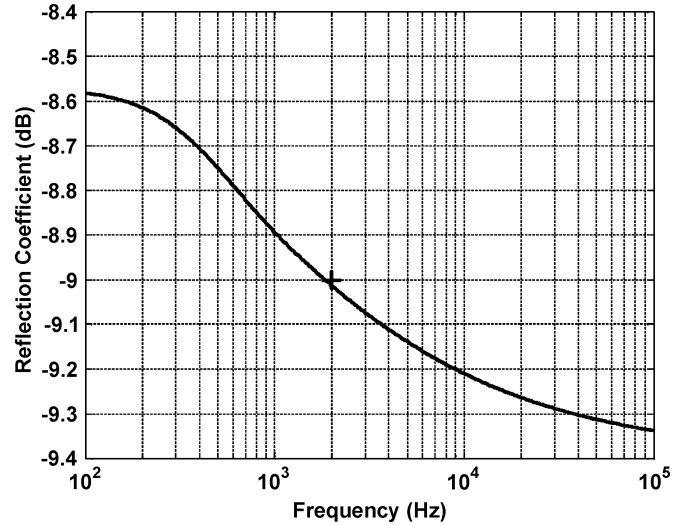


Fig. 22. Reflection coefficient as a function of frequency determined from inversion of chirp sonar data collected at the SAX-99 site. The + marks the reflection coefficient measurement of  $-9.0$  dB at 2 kHz.

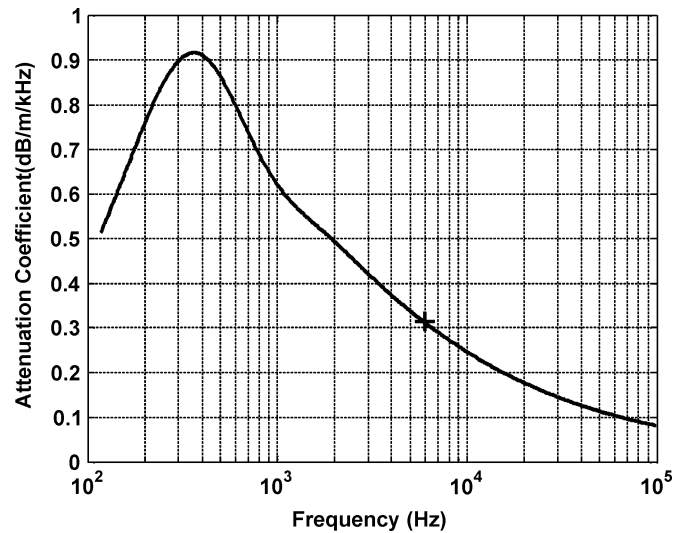


Fig. 23. Attenuation coefficient as a function of frequency determined from on inversion of chirp sonar data collected at the SAX-99 site. The + marks the attenuation rolloff measurement of 0.3155 dB/m/kHz at a center frequency of 6 kHz.

while the inversion of chirp sonar data provides the properties of the sediments above the selected subsurface reflector, which varied from 3 to 6 m below the sea floor.

Using the estimated values for porosity, mean grain size, and permeability in Table V, the Biot model input parameters are recalculated and the acoustic properties of the sediments are determined from (25) and (26). In Fig. 22, the reflection coefficient function (32) is plotted against frequency from 100 Hz to 100 kHz. The reflection coefficient measurement at  $-9.0$  dB at 2 kHz is plotted on the graph to compare the measurement and the solution. The Biot model solution for attenuation rolloff is plotted in Fig. 23 for the frequencies of 100 Hz to 100 kHz. The rolloff of 0.3155 dB/m/kHz at 6 kHz is plotted on the graph to compare the measurement and the solution.

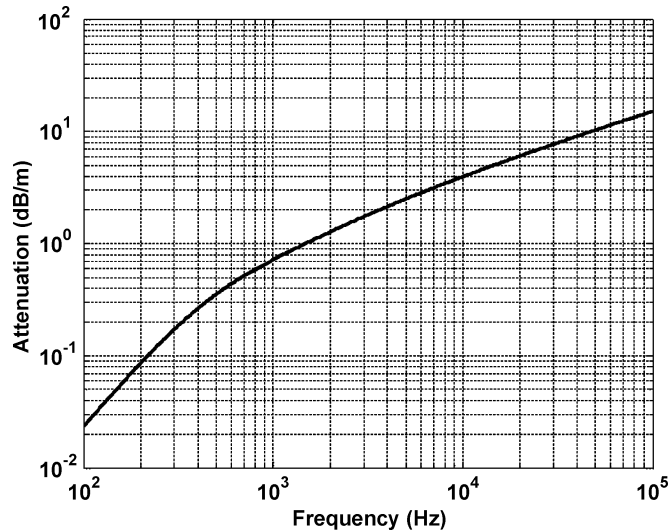


Fig. 24. Attenuation as a function of frequency determined from inversion of chirp sonar data collected at the SAX-99 site. This curve agrees with the attenuation function determined by Williams [4], who fits Biot model outputs to physical property data and *in situ* fast wave attenuation and velocity measurements collected at the SAX-99 site.

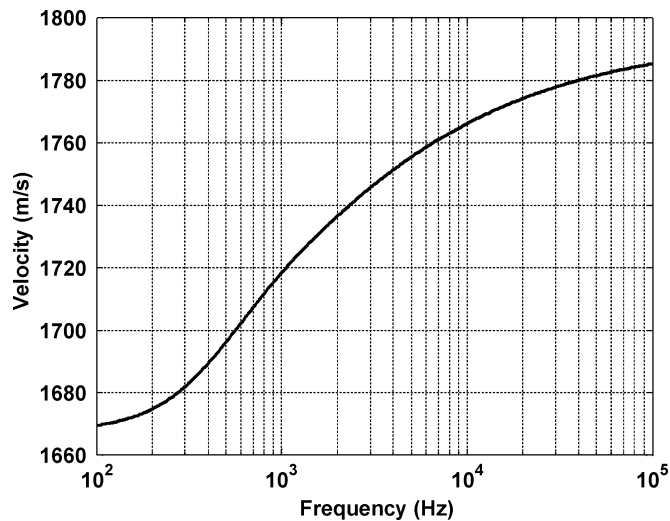


Fig. 25. Fast wave velocity as a function of frequency determined from inversion of chirp sonar data collected at the SAX-99 site. This curve agrees with the sound-speed function reported by Williams [4], who fits Biot model outputs to physical property data and *in situ* fast wave attenuation and velocity measurements collected at the SAX-99 site.

As shown in Fig. 23, the Biot model predicts that attenuation rolloff decreases as frequency increases near 6 kHz. This phenomenon is not seen in the attenuation rolloff measurements, which show that attenuation rolloff does not change significantly with frequency. A potential explanation is that as the slope of intrinsic attenuation (predicted by the Biot model) decreases with increasing frequency, attenuation losses associated with volume scattering losses are increasing with frequency. The intrinsic attenuation and the transmission loss due to volume scattering could be balanced such that the effective attenuation has a linear slope. In that case, the attenuation rolloff would be independent of frequency. This discrepancy may be resolved by increasing the bandwidth of the attenuation rolloff

measurements to detect the nonlinear trend in attenuation over a broader range of frequencies.

Figs. 24 and 25 show the attenuation and velocity of the fast wave generated using (25) and (26). The attenuation rolloff plotted in Fig. 23 is the slope of the attenuation function shown in Fig. 24. Fig. 24 and 25 closely match the attenuation and velocity functions derived by Williams [4], providing further support for the chirp sonar inversion. Williams calculated similar attenuation and velocity functions using the Biot model, physical property data and *in situ* attenuation and fast wave velocity measurements collected at the SAX-99 site.

## VI. CONCLUSION

The purpose of this paper is to investigate the possibility of using the Biot model for processing chirp sonar data in order to obtain sediment properties if no core data are available. The proposed inversion procedure uses the reflection coefficient and attenuation rolloff measurements to generate a unique solution for the porosity and permeability of sediments in the top sediment layer. A modified Kozeny–Carman equation uses the solution to estimate the mean grain size of those sediments. This technique makes a number of assumptions preventing its use in all depositional environments. First and foremost, a subsurface reflector must be present in the reflection data. If a subsurface reflection does not exist, the reflection coefficient is used to estimate the properties with large errors as shown in the second column of Table V. Second, the interface at the bottom of the top sediment layer must be a step change in impedance. Fine layering and scattering from sediment heterogeneities or from a transition layer where impedance changes gradually with depth causes interference in the echo spectrum, thereby precluding use of the inversion method. Another significant assumption is that permeability is proportional to the square of the pore-size parameter. Other assumptions are given in Table III and its discussion.

The inversion procedure generates estimates of porosity, permeability, and mean grain size for the SAX-99 site that agree with directly measured values as shown in Table V. Those property estimates are processed by the Biot model to generate estimates of attenuation and fast wave velocity functions. The functions that agree with results described by Williams [4]. However, a significant discrepancy exists between the chirp sonar attenuation rolloff measurement and that predicted by the Biot model. The attenuation rolloff measurement indicates that attenuation is linearly dependent on frequency near 6 kHz while the Biot model predicts that the attenuation rolloff, which is the slope of the attenuation function, should be decreasing with increasing frequency. The inversion assumes that the measured attenuation rolloff is identical to the slope of the intrinsic attenuation function predicted by the Biot model. The attenuation rolloff measurement may include an attenuation loss component due to volume scattering that could account for the discrepancy.

Given that the inversion method correctly estimated the physical and acoustic properties of sediments at the SAX-99 site using chirp sonar, water temperature and salinity data, and regional mineralogy (the quartz grain assumption), the inversion method has demonstrated its potential for estimating sea-bed

properties without taking sediment cores. However, much more field work is required to establish the accuracy and limitations of the inversion procedure and to refine the interrelationships of Table III for the wide range of depositional environments that exist in the ocean before the inversion method can be deployed for generating maps of sediment properties. If this method proves to be reliable at predicting the properties of the top sediment layer, the inversion method can be extended to calculate the properties of successively deeper sediment layers.

#### ACKNOWLEDGMENT

The author would like to thank J. Wulf, Chirp Sonar Laboratory Project Manager, who supervised the design, fabrication, and testing of the chirp sonar system deployed in the 2002 experiment at the SAX-99 site.

#### REFERENCES

- [1] E. L. Hamilton, "Reflection coefficients and bottom losses at normal incidence from Pacific sediment properties," *Geophys.*, vol. 35, pp. 995–1004, 1970.
- [2] N. P. Chotiros, A. P. Lyons, J. Osler, and N. G. Pace, "Normal incidence reflection loss from a sandy sediment," *J. Acoust. Soc. Amer.*, vol. 112, no. 5, pp. 1831–1841, 2002.
- [3] C. W. Holland and B. A. Brunson, "The Biot-Stoll sediment model: an experimental assessment," *J. Acoust. Soc. Amer.*, vol. 84, no. 4, pp. 1437–1531, 1988.
- [4] K. L. Williams, D. R. Jackson, E. I. Thorsos, D. Tang, and S. G. Schock, "Comparison of sound speed and attenuation measured in a sandy sediment to predictions based on the Biot theory of porous media," *IEEE J. Oceanic Eng.*, vol. 27, pp. 413–428, July 2002.
- [5] N. P. Chotiros, "Biot model of sound propagation in water-saturated sediment," *J. Acoust. Soc. Amer.*, vol. 97, no. 1, pp. 199–214, 1995.
- [6] —, "An inversion for Biot parameters in water-saturated sand," *J. Acoust. Soc. Amer.*, vol. 112, no. 5, pp. 1853–1868, 2002.
- [7] M. A. Biot, "Mechanics of deformation and acoustic propagation in porous media," *J. Appl. Phys.*, vol. 33, pp. 1482–1498, 1962.
- [8] R. Stoll, "Acoustic waves in ocean sediments," *Geophys.*, vol. 42, no. 4, pp. 715–725, 1977.
- [9] M. A. Biot, "Theory of propagation of elastic waves in a fluid-saturated porous solid. II. Higher frequency range," *J. Acoust. Soc. Amer.*, vol. 28, pp. 179–191, 1956.
- [10] R. T. Bachman, "Acoustic and physical property relationships in marine sediments," *J. Acoust. Soc. Amer.*, vol. 78, no. 2, pp. 616–621, 1985.
- [11] T. W. Lambe and R. V. Whitman, *Soil Mechanics*. New York: Wiley, 1969.
- [12] R. Soulsby, *Dynamics of Marine Sands*. London, U.K.: Thomas Telford, 1997.
- [13] A. H. Reed, K. B. Briggs, and D. L. Lavoie, "Porometric properties of siliciclastic marine sand: a comparison of traditional laboratory measurements with image analysis and effective medium modeling," *IEEE J. Oceanic Eng.*, vol. 27, pp. 581–592, July 2002.
- [14] L. J. Poppe, A. H. Eliason, J. J. Fredericks, R. R. Rendigs, D. Blackwood, and C. F. Polloni, "USGS east-coast sediment analysis—Procedures, database, and georeferenced displays," U.S. Geological Survey Open File Rep. 00-358, 2000.
- [15] J. M. Hovem and G. D. Ingram, "Viscous attenuation of sound in saturated sand," *J. Acoust. Soc. Amer.*, vol. 66, no. 6, pp. 1807–1812, 1979.
- [16] P. C. Carman, *Flow of Gases Through Porous Media*. New York: Academic, 1956.
- [17] M. Clennell, "Tortuosity: a guide through the maze," in *Developments in Petrophysics, Geo. Soc. Special Pub. 122*, M. A. Lovell and P. K. Harvey, Eds. London, U.K.: Geol. Soc., 1997.
- [18] F. A. L. Dullien, *Porous Media, Fluid Transport and Pore Structure*. San Diego, CA: Academic, 1992.
- [19] C. H. Juang and R. D. Holtz, "Fabric pore size distribution and permeability of sandy soils," *J. Geotech. Eng.*, vol. 112, no. 9, pp. 855–868, 1986.
- [20] —, "A probabilistic permeability model and the pore size density function," *Int. J. Num. Analyt. Methods Geomech.*, vol. 10, pp. 543–553, 1986.
- [21] E. C. Childs and N. Collis-George, "The permeability of porous materials," *Proc. R. Soc. London, A, Math. Phys. Sci.*, vol. 201, no. 1066, pp. 392–405, 1950.
- [22] I. Garcia-Bengochea, C. W. Lovell, and A. G. Altschgeffl, "Pore distribution and permeability of silty-clays," *J. Geotech. Eng. Div.*, vol. 105, no. GT7, pp. 839–856, 1979.
- [23] T. J. Marshall, "A relation between permeability and size distribution of pores," *J. Soil Sci.*, vol. 9, no. 1, pp. 1–8, 1958.
- [24] S. Forster, B. Bobertz, and B. Bohling, "Permeability of sands in the coastal areas of the Southern Baltic Sea: Mapping a grain-size related sediment property," *Aquatic Geochem.*, vol. 9, pp. 171–190, 2003.
- [25] A. Rusch, S. Forster, and M. Huettel, "Bacteria, diatoms and detritus in an intertidal sandflat subject to advective transport across the water-sediment interface," *Biochem.*, vol. 55, pp. 1–27, 2001.
- [26] T. Yamamoto and A. Turgut, "Acoustic wave propagation through a porous media with arbitrary pore size distributions," *J. Acoust. Soc. Amer.*, vol. 83, no. 5, pp. 1744–1751, 1988.
- [27] T. Yamamoto, M. V. Trevorrow, M. Badiy, and A. Turgut, "Determination of the seabed porosity and shear modulus profiles using a gravity wave inversion," *Geophys. J. Int.*, vol. 98, pp. 173–182, 1989.
- [28] P. R. Ogushwitz, "Applicability of the Biot theory. I. Low-porosity materials," *J. Acoust. Soc. Amer.*, vol. 77, no. 2, pp. 429–440, 1985.
- [29] R. D. Stoll, "Theoretical aspects of sound transmission in sediments," *J. Acoust. Soc. Amer.*, vol. 68, no. 5, pp. 1341–1350, 1980.
- [30] —, "Marine sediment acoustics," *J. Acoust. Soc. Amer.*, vol. 77, no. 5, pp. 1789–1799, 1985.
- [31] M. Richardson *et al.*, "Overview of SAX-99: Environmental considerations," *IEEE J. Oceanic Eng.*, vol. 26, pp. 26–53, Jan. 2001.
- [32] R. H. Bennett, M. H. Hulbert, C. Curry, H. P. Johnson, M. Hutnak, and K. J. Curry, "In situ permeabilities of selected coastal marine sediments," *IEEE J. Oceanic Eng.*, vol. 27, pp. 571–580, July 2002.
- [33] S. G. Schock, *Remote sediment estimates of physical and acoustic properties in the South China Sea using chirp sonar data and the Biot model*, vol. 29, pp. 1218–1230, Oct. 2004.



**Steven G. Schock** (M'86) was born in Warwick, R.I., in 1956. He received the B.S. degree from the U.S. Naval Academy, Annapolis, MD, in 1979 and the Ph.D. degree from University of Rhode Island, Narragansett, in 1989, both in ocean engineering.

After receiving the B.S. degree, he entered the U.S. Navy Nuclear Power Program and served as Weapons Officer on *USS Dallas* (SSN-700). Currently, he is a Professor of Ocean Engineering at Florida Atlantic University, Boca Raton, where he has been conducting research and teaching since

1989. His research interests include bottom interacting acoustics, sediment classification, sea-bed and buried-object imaging, and sonar design.

Dr. Schock is a Member of the Acoustical Society of America and the Marine Technology Society.